

Broadband Spectra Analysis of Three Energetic Millisecond Pulsars

Department of Physics, The University of Hong Kong, Pokfulam
Road, Hong Kong

Wang Wenchao

3030053350

Acknowledgements

This is acknowledgement.

Abstract

In the thesis, I mainly introduce our study on the high energy spectra of three millisecond pulsars which are PSR J0218+4232, PSR B1821-24 and PSR B1937+21. The *Fermi LAT* Pass 8 data was published in 2015 and has lots of advantages over the old Pass 7 data, such as increased effective area and wider energy range. Since the recent gamma-ray spectra analysis of the three MSPs are relatively old (in about 2014), I redo the gamma-ray spectra analysis of the MSPs with 4-year more *Fermi LAT* observation data and newly published Pass 8 data. As expected, I obtain better fit results for gamma-ray spectra of the three MSPs with smaller errors and larger test statistic values. Then I briefly introduce a pulsar emission model called two-layer model [5] and do numerical simulation to test the two-layer model using the new observation data. By minimizing the differences between the predictions of the two-layer model and the real data, I fit the independent parameters of the two-layer model, which is helpful to understand emission mechanisms of pulsars. I find that though the two-layer model is simple, it can generate broad-band spectra of pulsars which are very close to the observation data from *Fermi LAT* in most energy bands.

Contents

Acknowledgements	i
Abstract	ii
List of Figures	iii
List of Tables	iii
1 Introduction	10
1.1 Neutron Stars and Pulsars	10
1.2 Emission Mechanism of Pulsars	11
1.2.1 Magnetic Dipole Model	12
1.2.2 Synchrotron Radiation	13
1.2.3 Inverse-Compton radiation	16
1.2.4 Curvature Radiation	20

1.2.5	A Brief Introduction to Basic Gamma-ray Emission Process	22
1.3	Millisecond Pulsar	23
1.3.1	P- \dot{P} Diagram	23
1.3.2	Origin Of Millisecond Pulsars	25
1.3.3	Class II MSPs	26
1.4	Objectives	27
2	Gamma-Ray Analysis	28
2.1	Introduction to the <i>Fermi Gamma-ray Space Telescope</i>	28
2.2	A Brief Introduction to Fermi Data Analysis	31
2.3	<i>Fermi LAT</i> Data Analysis	34
2.3.1	Verifying the Data Analysis Process	35
2.3.2	PSR J0218+4232	37
2.3.3	PSR B1821-24	42
2.3.4	PSR B1937+21	46
3	Theory And Simulation	50
3.1	Two-layer Model	50
3.2	Numerical Calculation of Spectra Based on Two-layer Model . . .	56
3.3	Pitfalls and Considerations of Doing Numerical Calculation . . .	59

3.3.1	Correctness of Computation	59
3.3.2	Speed of Computation	62
4	Discussion and Future Work	64

List of Figures

1.1	Spatial distribution of some pulsars in galactic coordinate system.	11
1.2	Braking index of some pulsars.	13
1.3	Spectrum shape of synchrotron radiation for a single particle (top). According to Eq. 1.6, The top figure 1.6 describes the general shape of power spectrum of synchrotron radiation. When the frequency is larger than the critical frequency ν_c , the power goes down dramatically. However, the top figure does not show the information that at what frequency the charged particle emit the strongest power, which can be described in the bottom figure. The bottom figure reveals that most energy is emitted around critical frequency.	15
1.4	Inverse Compton Diagram	17
1.5	Two photons collide with an electron. In the frame S' , two photons collide with a rest electron successively. In the frame S , the electron is no longer at rest and the positions of the two events are x_1 and x_2	21
1.6	Position of pulsars in P- \dot{P} diagram	24

1.7	A schematic diagram of Roche lobe. L_1 is called inner Lagrange point which is the intersection of equipotential lines of star A and B.	25
1.8	Pulse profiles of PSR B1937+21 in radio, X-ray and gamma-ray. [5]	26
2.1	The figure (https://www-glast.stanford.edu/instrument.html) illustrates how <i>Fermi LAT</i> tracks incident gamma-ray photons. .	29
2.2	The count map of PSR J0218+4232 (left) and the count map generated by the model (right). In the left panel, the green circles represent free sources. Fig. in the right is a count map created according to our fitted spectra model. The size of each figure is 141 pixels \times 141 pixels, and the dimension for each pixel is $0.2^\circ \times 0.2^\circ$	38
2.3	Three count maps from PSR J0218+4232's count cube. The energy ranges of the figures are 100~123MeV, 1.873~2.310GeV, 35.11~43.29GeV respectively.	38

- 2.4 The count map and residual map of PSR J0218+4232. The figures are both in linear scale in order to compare the residual map between the original count map more intuitively. The left panel is the count map and the right one is the residual map which shows the differences between the observation and the spectral model. It is created by directly subtracting the photon counts of each pixel between the count maps of observation data and the spectral model. The green circle regions represent (the regions are completely the same in the two figures) the largest number photon counts of the residual map and its radius is $2000''$. 40
- 2.5 The log-log plot of flux to energy of PSR J0218+4232. The grey shade represents fitting errors, black points with error bars are flux points, the blue dots are upper values and the red line is the PLExpCutoff model multiplied by E^2 . Flux points are fitted separately by dividing the total energy bin ($100 \text{ MeV} \sim 100 \text{ GeV}$) into multiple energy bins. The horizontal error bars represents the width of each bin. 42
- 2.6 TS maps of PSR J0218+4232. Figures' dimensions are $4^\circ \times 4^\circ$ ($20 \text{ pixels} \times 20 \text{ pixels}$ with $0.2^\circ \times 0.2^\circ$ for each pixel). The left figure and right figure are generated by the XML models with and without our target source PSR J0218+4232 respectively. The left figure shows that the possibility of adding an imputative point source is very low only with a maximum TS value of less than 5. However, the right figure strongly implies that there should be an additional source after we have removed our target source from the spectral model, which means it's highly likely that PSR J0218+4232 is contained in our observation data. . . . 43

2.7	The count map of PSR B1821-24 (left) and the count map generated by the model (right). In the left panel, the green circles are free sources. The sizes of the both figures are $141 \text{ pixels} \times 141 \text{ pixels}$, and each pixel's dimension is $0.2^\circ \times 0.2^\circ$	43
2.8	Three figures of PSR B1821-24's count cube. The energy ranges of the figures are $100 \sim 123 \text{ MeV}$, $1.873 \sim 2.310 \text{ GeV}$, $81.11 \sim 100 \text{ GeV}$ respectively from left to right.	44
2.9	The count map and residual map of PSR B1821-24 in log scale. The reason why linear is not used here is that the residual map is nearly black in linear scale. The left figure is the count map and the right figure is the residual map showing the difference between the observation data and the spectral model.	44
2.10	The log-log plot of flux to energy of PSR B1821-24's gamma-ray spectrum.	45
2.11	TS maps of PSR B1821-24. The figures' dimensions are $4^\circ \times 4^\circ$ ($20 \text{ pixels} \times 20 \text{ pixels}$ with $0.2^\circ \times 0.2^\circ$ for each pixel). The left figure and right figure are generated by the XML models with and without our target source PSR B1821-24 respectively. The left figure shows that the possibility of adding an imputative point source is very low only with a maximum TS value of less than 11 while the TS values of the right figure are generally much larger.	47
2.12	The count maps of PSR B1937+21 are created from observation data (left) and from the spectral model (right) respectively. The dimensions of both figures are $141 \text{ pixels} \times 141 \text{ pixels}$ and each pixel is $0.2^\circ \times 0.2^\circ$ large.	47

2.13	Three figures of PSR B1937+21's count cube. The energy ranges of the figures are 100~123MeV, 1.873~2.310GeV, 35.11~43.29GeV respectively.	49
2.14	here	49
2.15	The count maps of PSR B1937+21 created from observation data (left) and from the spectral model (right). The dimensions of both figures are $141pixels \times 141pixels$ and each pixel's size is $0.2^\circ \times 0.2^\circ$	49
3.1	(a): Geometry of the two-layer model. h_1 and h_2 is the height of the primary region and the screening region respectively. (b): the charge densities of primary region and screening region. In the primary region, the charge density is much smaller than Goldreich-Julian charge density while is larger in the screening region.	51
3.2	The modeled spectrum of PSR J0218+4232.	57
3.3	The modeled spectrum of PSR B1821-24.	58
3.4	The modeled spectrum of PSR B1937+21.	58
3.5	The broad band and modeled spectrum of PSR J0218+4232. The grey shade is the error of the global fit. And the green shade in the left panel of the figure represents the error of hard X-ray. The 'Total' legend represents the total flux combining the Synchrotron radiation, inverse Compton radiation and curvature radiation altogether.	60

3.6	The broad band and modeled spectrum of PSR B1821-24. The meaning of grey shade and the green shade are the same as Fig. 3.5	60
3.7	The broad band and modeled spectrum of PSR B1937+21. The meaning of grey shade and the green shade are the same as Fig. 3.5	61

List of Tables

2.1	The spectra fit results. In the thesis, in order to make data analysis more convinient, we use some pipeline scripts to deal with the observation data. The "Test Results" column shows the results generated by using the pipeline scripts. The "Previous Results" column lists the corresponding spectra properties based on the old paper [1]. According to the standard PLSuperExpCutoff model (described in equation 2.4, Γ is photon index and E_c is cutoff energy.)	36
2.2	Fit Results With Data From Year 2009 To Year 2018. The physical meanings of Γ and E_c are the same as Table 2.1.	37
2.3	Numbers of photon counts of count maps in different energy bands for PSR J0218+4232.	39
2.4	Fit parameters of the spectral model of PSR J0218+4232. The names of parameters are consistent with Eq. 2.4. The old results are from the paper [1].	41

2.5	Fit parameters of the spectral model of PSR B1821-24. The names of parameters are also onsistent with Eq. 2.4 We should note that the energy ranges of photon flux between the two results are different. The energy is from 100MeV to 100GeV for the new results while from 200MeV to 300GeV for the previous results.	46
3.1	The results of fitting parameters for the three MSPs. The physical meaning of each parameter is consistent with the two-layer model describe above.	59

Chapter 1

Introduction

1.1 Neutron Stars and Pulsars

Neutron stars are produced by supernovae explosion of massive stars which have about four to eight solar mass. After a supernova explosion, a star leaves a central region. And the central region collapses because of the effect of gravity until protons and electrons combine to form neutrons ($e^- + p \rightarrow n + \nu_e$)—the reason why they are called “neutron stars”. Because neutrons have no electromagnetic force on each other, they can be squeezed very tightly. Therefore, a neutron star has tremendous high density (about $5 \times 10^{17} \text{kg/m}^3$) and its diameter and mass is about 20km and 1.4 solar mass respectively. What prevents a neutron star to continue to contract is the degeneracy pressure of neutrons.

Pulsars are fast-spinning neutron stars. They have rotational periods from a few milliseconds to several seconds. For example, the rotational period of PSR B1937+21 is about 1.56ms while PSR B1919+21 is approximately 1.34s. As we know, a star can be ripped by centrifugal force if the star rotates too fast.

We can estimate lower limit of density of a star with the equation $\rho = \frac{3\pi}{P^2 G}$, where P is the rotational period of a pulsar. Just for simplicity, let P be 1s. Then we get $\rho \approx 1.4 \times 10^{11} \text{kg/m}^3$. With the knowledge that the density of a white dwarf is about $1 \times 10^9 \text{kg/m}^3$ which is smaller than the lower density limit, the observed fast-spinning stars belong to the kind of stars which are much denser than white dwarf. As a result, neutron stars are ideal candidates for pulsars.

More than 2000 pulsars have been discovered so far. Most of them are in the disk of our Galaxy while we also can find a small portion of them in high latitude, which can be seen clearly in Fig. 1.1. This may because they cannot escape the gravitational potential if their kinetic energy is not large enough. Besides, even though they have large enough velocities to escape from their birth region, there are some probabilities that they become nearly non-detectable before reaching high latitude.

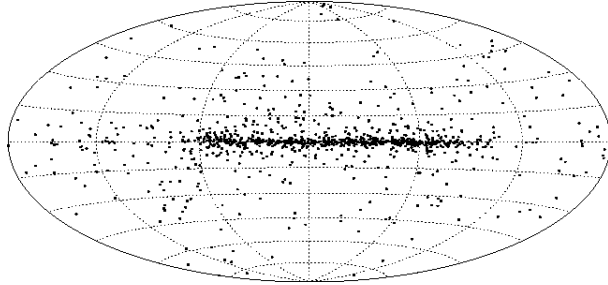


Figure 1.1: Spatial distribution of some pulsars in galactic coordinate system.

1.2 Emission Mechanism of Pulsars

Although the emission mechanism of pulsars has not been fully understood yet, some models have been developed trying to explain observational data. The following is a simple model that can explain some basic features of pulsars spectra. I will first introduce the magnetic dipole model, then the synchrotron

radiation and inverse Compton radiation.

1.2.1 Magnetic Dipole Model

Assuming a pulsar has a magnetic dipole moment \vec{m} , the angel between rotation axis and direction of \vec{m} is α , its angular velocity is Ω , radius is R and moment of inertia is I . Also assuming that energy of electromagnetic radiation is completely from the rotational energy, its spin-down rate can be written as:

$$\dot{\Omega} = -\frac{B_p^2 R^6 \Omega^3 \sin^2 \alpha}{6c^3 I}$$

where B_p is magnetic field strength in the pole of the pulsar. Its surface magnetic field can also be estimated by:

$$B_s = \sqrt{\frac{3c^3 I}{2\pi^2 R^6} P \dot{P}} = 3.2 \times 10^{19} \sqrt{P \dot{P}}$$

where B_s is the strength of surface magnetic field.

In general, a pulsar's spin down rate can be expressed as: $\dot{\Omega} = -K\Omega^n$, where K is a constant and n is called braking index. In magnetic dipole model n is 3 [8]. Then characteristic age of the pulsar can be defined as: $P/2\dot{P}$ in magnetic dipole model. For example, the Crab pulsar's rotation period is about 0.033s and period derivative is $4.22 \times 10^{-13} s/s$. The characteristic age is about 1200 years. The pulsar is remnant of a supernova which is observed by ancient astronomers in 1054 AD, so the record shows that characteristic age can give us an order of magnetic estimate of a pulsar's real age.

Although the braking index is 3 in magnetic dipole model, most of pulsars' braking index is less than 3 as shown in Fig. 1.2. The reason is that if a pulsar's spin down is completely because of pulsar wind, the braking index is 1. Thus, the real braking index should be a combination of 1 and 3, which is

usually less than 3. [4]

Pulsar	n_{obs}	Ω s^{-1}	$\dot{\Omega}$ 10^{-10}s^{-2}
PSR B0531+21 (Crab)	2.51 ± 0.01	30.22543701	-3.862283
PSR B0540-69	2.14 ± 0.01	19.8344965	-1.88383
PSR B0833-45 (Vela)	1.4 ± 0.2	11.2	-0.157
PSR B1509-58	2.839 ± 0.001	6.633598804	-0.675801754
PSR J1846-0258	2.16 ± 0.13	3.0621185502	-0.6664350
PSR J1833-1034	1.857 ± 0.001	16.159357	-0.5275017
PSR J1119-6127	2.684 ± 0.001	2.4512027814	0.2415507
PSR J1734-3333	0.9 ± 0.2	0.855182765	-0.0166702

Figure 1.2: Braking index of some pulsars.

1.2.2 Synchrotron Radiation

Synchrotron radiation is a special case of cyclotron radiation when particles' speed is comparable to the speed of light. Because of the relativistic beaming effect, we will observe a very short radiation pulse when speed of particles is large. We only aim to analyze the spectral properties of MSPs, so we focus on the spectrum property of synchrotron radiation. With Larmor's Formula we can derive the synchrotron radiation power of an electron:

$$P = \frac{2e^4\gamma^2\beta^2 B_{\perp}^2}{3m_e^2 c^3} \quad (1.1)$$

where γ is the Lorentz factor of the electron, $\beta = v/c$ and B_{\perp} is the strength of magnetic field perpendicular to the circular motion plane. When $\beta \sim 1$, Function 1.1 can be simplified as:

$$P = \frac{2}{3} \frac{e^2 c}{R^2} \gamma^4 \quad (1.2)$$

where $R = E/eB_{\perp}$ is the radius of the electron's circular motion. Furthermore, the power spectrum of a single electron can be described by Function 1.3

$$\begin{aligned} P(\nu) &= \frac{\sqrt{3}e^3 B \sin \alpha}{mc^2} \left(\frac{\nu}{\nu_c} \right) \int_{\nu/\nu_c}^{\infty} K_{5/3}(\eta) d\eta \\ &= \frac{\sqrt{3}e^2}{m_e R} \gamma \left(\frac{\nu}{\nu_c} \right) \int_{\nu/\nu_c}^{\infty} K_{5/3}(\eta) d\eta \end{aligned} \quad (1.3)$$

where ν_c is the critical frequency and $K_{5/3}$ is modified Bessel function. The critical frequency can be expressed by Function 1.4

$$\begin{aligned} \nu_c &= \frac{3}{2} \gamma^2 \nu_{cyc} \sin \alpha \\ &= \frac{3}{4\pi} \frac{c}{R} \gamma^3 \end{aligned} \quad (1.4)$$

where α is the pitch angle and the ν_{cyc} is the frequency of corresponding cyclotron radiation. These functions do not give us very much information because of the integration of the modified Bessel function. We let $x = \nu/\nu_c$ and fix the environment variables such as magnetic field (B), Function 1.3 becomes:

$$P(\nu) = C \times x \int_x^{\infty} K_{5/3}(\eta) d\eta \quad (1.5)$$

where C is a constant dependent on B . Thus, in order to analyze the power spectrum of synchrotron radiation, we only concentrate on the later part, which is

$$F(x) = x \int_x^{\infty} K_{5/3}(\eta) d\eta \quad (1.6)$$

In reality, synchrotron radiation is not generated by a single particle. We describe the number density distribution of electrons with respect to energy by a single power-law model:

$$N(E) \approx CE^{-\delta} \quad (1.7)$$

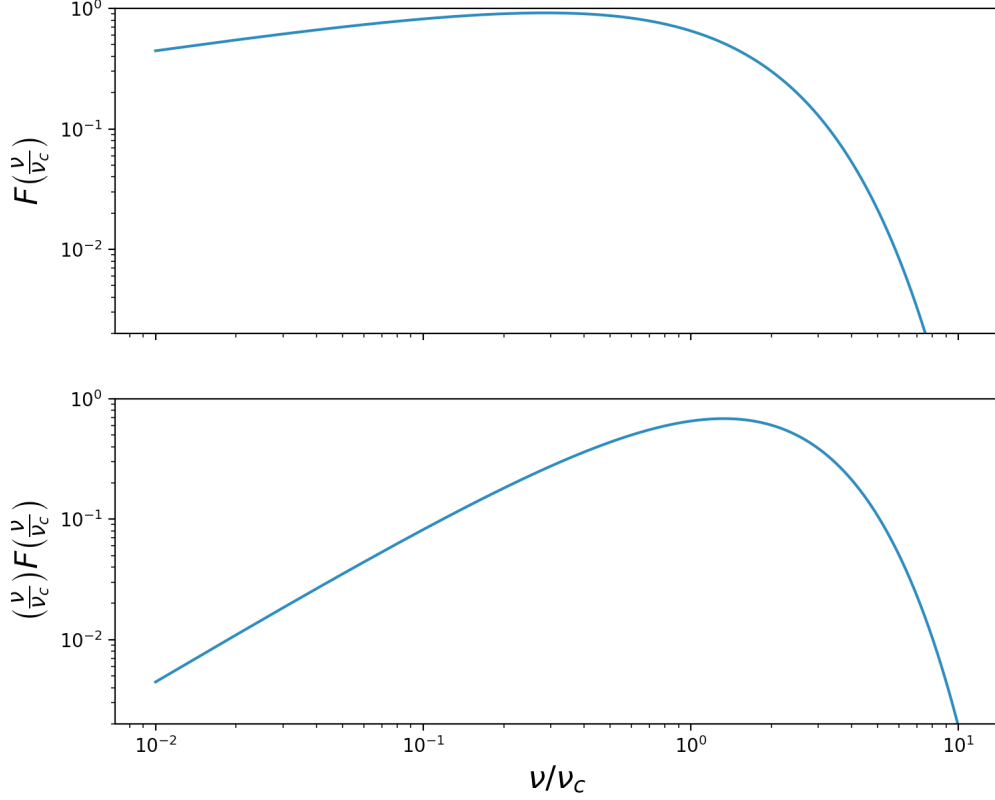


Figure 1.3: Spectrum shape of synchrotron radiation for a single particle (top). According to Eq. 1.6, The top figure 1.6 describes the general shape of power spectrum of synchrotron radiation. When the frequency is larger than the critical frequency ν_c , the power goes down dramatically. However, the top figure does not show the information that at what frequency the charged particle emit the strongest power, which can be described in the bottom figure. The bottom figure reveals that most energy is emitted around critical frequency.

For simplicity, we set the ambient magnetic field B to be a constant and make an approximation that all radiations are at a single frequency:

$$\nu \approx \gamma^2 \nu_{cyc} \quad (1.8)$$

where the meaning of ν_{cyc} is the same as Function 1.4. Our objective is to know the relationship between total power of all electrons and their radiation frequency. We describe the relationship as Eq. 1.9

$$-P(E) N(E) dE = Q_\nu d\nu \quad (1.9)$$

$$P(E) = \frac{4}{3} \sigma_T \beta^2 \gamma^2 c U_B \quad (1.10)$$

where σ_T is electron Thompson scattering section, U_B is energy density of the environment magnetic field, Q_{nu} is the emission coefficient of synchrotron radiation and $E = \gamma m_e c^2$. With Eq. 1.8, we have

$$P = \frac{dE}{d\nu} = \frac{m_e c^2}{2\sqrt{\nu\nu_{cyc}}} \quad (1.11)$$

Combine Functions 1.11 and 1.9 we get:

$$Q_\nu = \frac{4}{3} \sigma_T \beta^2 \gamma^2 c U_B \frac{m_e c^2}{2\sqrt{\nu\nu_{cyc}}} N(E) \quad (1.12)$$

Ignoring constants in Function 1.9 we have

$$Q_\nu \propto \nu^{(1-\delta)/2} \quad (1.13)$$

Function 1.13 shows that if the number density electrons is a power-law distribution, the spectrum of synchrotron radiation is also a power-law model.

1.2.3 Inverse-Compton radiation

If an energetic relativistic photon collides with a charged particle from an proper incident angle, the photon's energy decreases and its direction changes. This is the process of Compton Scattering. Inverse-Compton radiation is the opposite process and a low energy photon gained energy from an ultra-relativistic electron in the process.

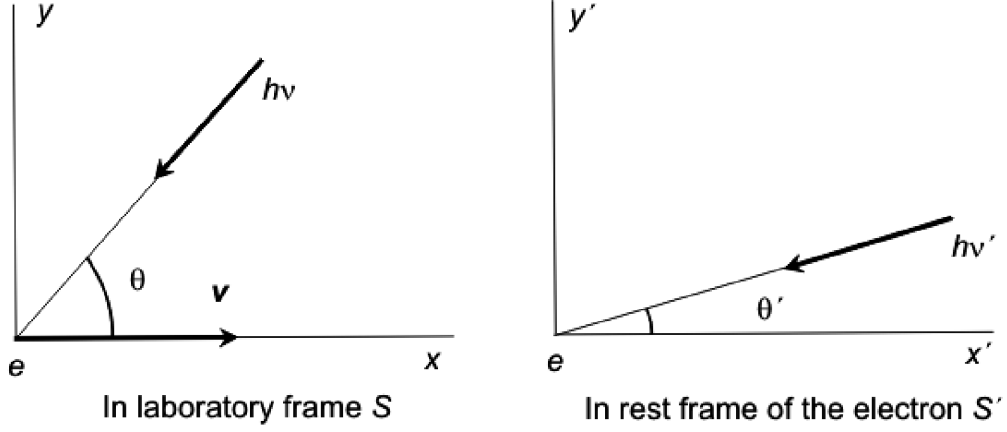


Figure 1.4: Inverse Compton Diagram

As Fig. 1.4 shows, in the laboratory frame (S), the incident angle and energy of a photon is θ and $h\nu$ respectively. The speed of the electron is v . In the electron rest frame (S'), we change the denotation to θ' , $h\nu'$ and. Also, let the position of the electron be the origin point of S' . We can study the whole process in the S' frame, the transfer the result to the S frame by Lorentz transformation.

In the S' frame, the electron is at rest so its energy is $m_e c^2$. For Inverse Compton scattering, the energy of an incident photon (less than several keV) is much less than the rest energy of an electron (about $0.51MeV$) and the relationship can be expressed by $h\nu' \ll m_e c^2$. Therefore, this can be treated as Thompson Scattering process. Let the Poynting vector of incident photons be \vec{S}' and their energy density be U'_{rad} , we have equation 1.14

$$\vec{S}' = cU'_{rad} \quad (1.14)$$

The electron absorbs the energy of the incident photons and then be accelerated. Thus the accelerated electron will emit part of the energy taken from incoming photons and the power of scattered radiation is denoted as P' . The

ratio can be described by Thompson Scattering cross section σ_T which is:

$$\sigma_T = \frac{8\pi}{3} \left(\frac{e^2}{m_e c^2} \right)^2 \quad (1.15)$$

and the relationship between the electron radiation power and incoming photon energy flux can be described by Eq. 1.16

$$P' = \left| \vec{S}' \right| \sigma_T \quad (1.16)$$

Combine Eqs. 1.14 and 1.16, the radiation power emitted by the electron is:

$$P' = c \sigma_T U'_{rad} \quad (1.17)$$

Then we need to find the relationship between frames S and S' . It mainly contains two parts: the relationship between P , P' and U_{rad} , U'_{rad} . Since $P = dE/dt$ and dE/dt is Lorentz invariant in inertial frame, we get the equation:

$$P = P' \quad (1.18)$$

Now we hope to write U'_{rad} in terms of U_{rad} . U_{rad} is comprised by energy of a single photon and photon density. In the following analysis, all the denotations are correspondent to Eq. 1.4. According to the relativistic Doppler shift formula, we have:

$$h\nu' = (h\nu) \gamma (1 + \beta \cos \theta) \quad (1.19)$$

where $\beta = v/c$ and γ is Lorentz factor of an ultra-relativistic electron. Then we calculate the photon density. In the frame S' , the photon density is inverse proportional to the time interval (Δt) between the two photons striking the electron since total number of photons is Lorentz invariant. In laboratory

frame S , we consider two photons collide with the electron at the 4-dimension vector of $(x_1, 0, 0, t_1)$ and $(x_2, 0, 0, t_2)$. According to the Lorentz transformation between inertial frames:

$$\left\{ \begin{array}{l} x = \gamma(x' + \beta ct') \\ y = y' \\ z = z' \\ t = \gamma\left(t' + \frac{\beta x'}{c}\right) \end{array} \right. \quad (1.20)$$

and because we set $x' = 0$, from Eq. 1.20, the two events of two successive photons collide with the electron can be expressed as: $(\gamma vt'_1, 0, 0, \gamma t'_1)$ and $(\gamma vt'_2, 0, 0, \gamma t'_2)$. As Fig. 1.5 shows, the time interval of two successive photons (reciprocal of frequency) in frame S is:

$$\begin{aligned} \Delta t &= (t_2 - t_1) + \frac{(x_2 - x_1) \cos \theta}{c} \\ &= \gamma(t'_2 - t'_1) + \frac{\gamma v(t'_2 - t'_1) \cos \theta}{c} \\ &= \Delta t' \gamma (1 + \beta \cos \theta) \end{aligned} \quad (1.21)$$

Eq. 1.21 shows that the relationship of photon number density between frame S and S' is:

$$n' = n \gamma (1 + \beta \cos \theta) \quad (1.22)$$

Combine Eqs. 1.22 and 1.19 we can transfer the incident photon energy density from frame S to S' according to Eq. 1.23

$$U'_{rad} = U_{rad} [\gamma (1 + \beta \cos \theta)]^2 \quad (1.23)$$

In Eq. 1.23, the incoming photon energy density is a function of the incident angle (θ), in order to get the total photon energy density, we integrate the

equation over θ . Then we get:

$$U'_{rad} = \frac{4}{3}U_{rad} \left(\gamma^2 - \frac{1}{4} \right) \quad (1.24)$$

Combine Eqs. 1.24 and 1.17, the total scattered radiation power is:

$$\begin{aligned} P' &= P \\ &= \frac{4}{3}\sigma_T c U_{rad} \left(\gamma^2 - \frac{1}{4} \right) \end{aligned} \quad (1.25)$$

As mentioned before, P' and P are the total radiation powers after scattering. Before the low energy gain photons, they give away some energy first which is $\sigma_T c U_{rad}$. Therefore, we have to subtract this value from Eq. 1.25 to calculate the rate of net energy gain, which is described by Eq. 1.26.

$$\begin{aligned} P' = P = \frac{dE}{dt} &= \frac{4}{3}\sigma_T c U_{rad} \left(\gamma^2 - \frac{1}{4} \right) - \sigma_T c U_{rad} \\ &= \frac{4}{3}\sigma_T c U_{rad} \beta^2 \gamma^2 \end{aligned} \quad (1.26)$$

If we compare Eq. 1.26 with Eq. 1.11, we find that the form is very similar between these two equations.

$$\frac{P_{IC}}{P_{sync}} = \frac{U_{rad}}{U_B} \quad (1.27)$$

where U_B is the energy density of environment magnetic field.

1.2.4 Curvature Radiation

Curvature radiation is the main source of gamma-ray photons. Charged particles not only move around magnetic field lines (synchrotron radiation), but

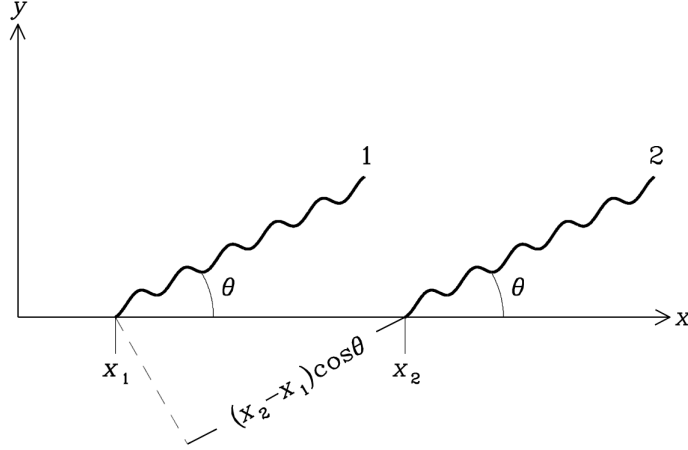


Figure 1.5: Two photons collide with an electron. In the frame S' , two photons collide with a rest electron successively. In the frame S , the electron is no longer at rest and the positions of the two events are x_1 and x_2

also along magnetic field lines (curvature radiation) because the magnetic field is very strong.

Eq. 1.1 shows that total synchrotron radiation power is related to pitch angel (because of the term B_{\perp}), and if the pitch angel is 0, there will be no synchrotron radiation. However, curvature radiation can still be generated and is dependent on the curvature radii of magnetic field lines:

$$P = \frac{2}{3} \frac{e^2 c}{s^2} \gamma^4 \quad (1.28)$$

where s is the curvature radii of magnetic field lines. Eq. 1.28 is very similar to the Eq. 1.2 and the only difference is that R is changed to s . Similarly, according to the Eq. 1.3, the power spectrum of curvature radiation can be written as:

$$P = \frac{\sqrt{3}e^2}{m_e s} \gamma \left(\frac{\nu}{\nu_c} \right) \int_{\nu/\nu_c}^{\infty} K_{5/3}(\eta) d\eta \quad (1.29)$$

where ν_c is the critical frequencies of curvature photons and equals to:

$$\nu_c = \frac{3}{4\pi} \frac{c}{s} \gamma^3 \quad (1.30)$$

According to Eqs. 1.28, 1.29 and 1.30, the spectral properties of curvature radiation are similar to synchrotron radiation. The only differences in the equations are particles' Lorentz factors and curvature radii.

1.2.5 A Brief Introduction to Basic Gamma-ray Emission Process

It is oversimplified to regard a pulsar as a magnetized sphere rotating in vacuum. Actually, there are plenty of charged particles in a pulsar's magnetosphere which co-rotate with the pulsar. The creation of charged particles can be described by the following steps [7].

1. The co-rotating charged primary particles emit gamma-ray by curvature radiation because of the acceleration in super strong magnetic field.
2. In intense magnetic field, the high energy photons decay into electrons and positrons which are called secondary particles by the process: $\gamma + (B) \rightarrow e^+ + e^- + (B)$. Synchrotron photons can be emitted by these secondary particles.
3. Secondary particles are also accelerated to high speed in strong magnetic field just like primary particles and some of them then emit gamma-rays which can further decay into electrons and positrons. As a result, these charged particles can create more secondary particles.
4. This chain of process is quite efficient to produce charged particles and make a pulsar's magnetosphere filled with plasma as a consequence. Therefore, it is natural to study the distribution of charges in pulsar's magnetosphere. A characteristic charge density $\rho_{GJ} = -\frac{\vec{\Omega} \cdot \vec{B}}{2\pi c}$ is called Goldreich-Julian density. The charge density can offset part of electric

field (E_{\parallel}) which is parallel to magnetic field. There is a region in the magnetosphere called “outer gap” where ρ_{GJ} is so small that it can’t screen E_{\parallel} effectively. As a result, the charged particles can be accelerated to a very large velocity (Lorentz factor $\gamma \sim 10^7$) and then emit gamma-ray. Photons in outer gap can also create electrons and positrons by the process: $\gamma + \gamma \rightarrow e^- + e^+$. At the outer gap, the above process can’t happen because magnetic field is too weak in this region.

1.3 Millisecond Pulsar

1.3.1 P- \dot{P} Diagram

P - \dot{P} diagram is an important tool for analyzing evolutions of pulsars. Period (P) and time derivative of period (\dot{P}) are two of pulsars’ important characteristics. Analyzing the position of a pulsar in the P - \dot{P} diagram can give us some valuable information such as which evolution stage the pulsar is in or the type of the pulsar, etc. Fig. 1.6 is an example of a P - \dot{P} diagram. The horizontal axis is pulsars’ rotation periods and the vertical axis is time derivative of rotation periods (\dot{P}). In this P - \dot{P} diagram, the negative slope lines represent the strengths of surface magnetic fields while the positive slope lines represent the characteristic ages of pulsars. The following is a short explanation for this. From previous discussion, we have known that the characteristic age of a pulsar is $\tau = -P/\dot{P} = P/(-\dot{P})$, so line of constant τ is a set of straight lines with equal positive slope. We also know $B \propto \sqrt{P\dot{P}}$, therefore the line of constant B should be a part of hyperbola. However, a P - \dot{P} diagram is usually in log-log scale. Hence, if we let $P' = \log P$ and $\dot{P}' = \log \dot{P}$, $B \propto \sqrt{P\dot{P}}$ turns to $B \propto 1/2 (P' + \dot{P}')$, which represents a straight line.

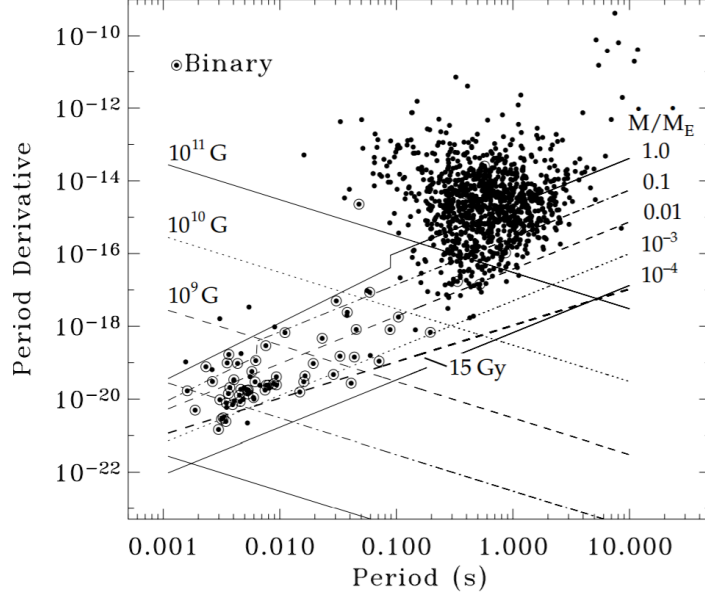


Figure 1.6: Position of pulsars in P - \dot{P} diagram

Fig. 1.6 shows that most pulsars lie in the position of about 1s, 10^{-14} s/s. At the same time, a couple of stars lie at the bottom-left of Fig. 1.6 — these are millisecond pulsars (MSPs). Their rotation periods are about 1-20 milliseconds. It is believed that MSPs are spun up by accretion of mass from their companion stars. In the above P - \dot{P} diagram, we can observe that millisecond pulsars' surface magnetic fields are about three to four orders of magnitude lower than those of normal pulsars. However, an MSP has a relative strong magnetic field near its light cylinder. The reason is that an MSP's radius of light cylinder ($R_{lc} = c/\omega$) is much smaller than a normal pulsar's because of its short rotation period and the magnetic field near light cylinder can be estimated as $B_{lc} \sim (R/R_{lc})^3$. At the same time, pulsars' emission mechanism is closely related to their magnetic field near the light cylinder. As a result, like a normal pulsar, an MSP also can have broadband spectrum from radio to gamma rays.

1.3.2 Origin Of Millisecond Pulsars

From pulsars' emission mechanisms, we know that magnetic field of a pulsar decreases with time while the spin period increase with time. But MSPs' spin periods are much shorter than normal pulsars and surface magnetic fields are a lot weaker. This makes an MSP seem to be both young and old. As a result, people think millisecond pulsars are old pulsars spun up by their companions. The companion stars transfer mass and angular momentum to accelerate the rotation speed of pulsar. Therefore, the aged pulsar can spin faster gradually.

Mass Transfer And Accretion In Binary Systems

X-ray binaries are a type of binary systems that is luminous in X-ray band. There are several kinds of X-ray binaries including low mass X-ray binaries (LMXB) and high mass X-ray binaries (HMXB). The mechanism of transferring mass is different in these two types of systems. Before discussing mass transfer, we need to know a little bit about Roche Lobe. Fig. 1.7 is a schematic diagram of Roche Lobe. We call two stars in an LMXB as A and B respec-

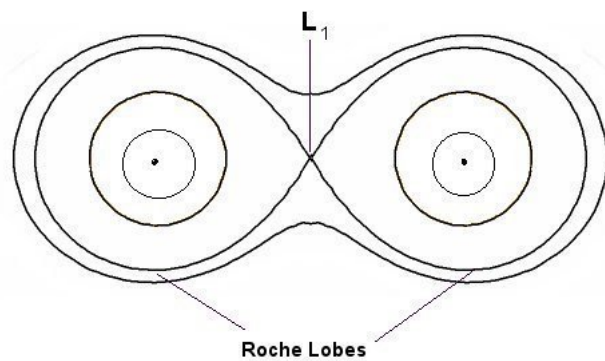


Figure 1.7: A schematic diagram of Roche lobe. L_1 is called inner Lagrange point which is the intersection of equipotential lines of star A and B.

tively for convenience. It is obvious that if an object is close to star A, the

gravitational influence of A is so strong that we can nearly ignore the effect of the star B. Similarly, this is true for star B. As a result, there must be a point where the effect of star A is equal to star B which is called inner Lagrange point [6]. The two parts inside the largest equipotential lines of A and B are called Roche lobe. If star B crosses its Roche lobe, then its mass will be attracted by A thus mass transfer between A and B happens. We should notice that this is the main way of mass transfer in LMXB. While in HMXB, the mass can be transferred by strong wind of the massive companion star.

What should be noted is that mass transfer can change the distance between two companion stars. If a low-mass star transfer mass to a high-mass companion star, the orbital separation will become larger. This can actually stop mass transfer and is a negative feedback. On the contrary, mass transfer from high-mass star to low-mass star will shrink the orbital distance.

1.3.3 Class II MSPs

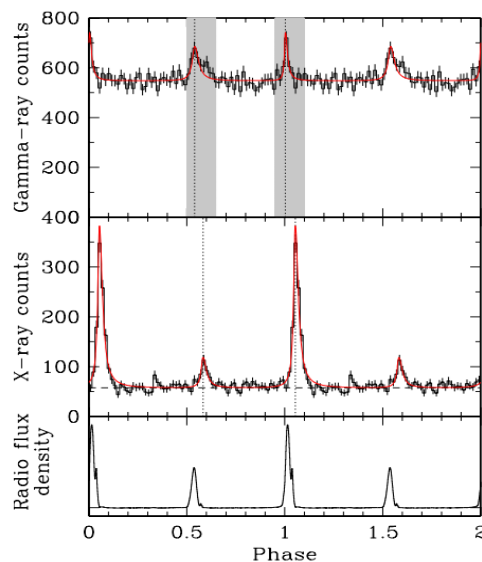


Figure 1.8: Pulse profiles of PSR B1937+21 in radio, X-ray and gamma-ray. [5]

Radio emissions are usually considered to be emitted above the polar cap,

which means radio emissions and gamma-ray emissions are from different location of a pulsar's magnetosphere. However, there are about 10 sources showing aligned pulse profiles in radio and gamma-ray implying that radio emission may produced from outer magnetosphere and they are called Class II MSPs [3]. These pulsars have strong magnetic fields near the light cylinder. Fig. 1.8 is an example of aligned pulse profile.

1.4 Objectives

Three millisecond pulsars J0218+4232, B1821-24 and B1937+21 show broadband spectra across radio, X-ray and gamma-ray bands. *Fermi LAT* gives us additional data and tools to do gamma-ray analysis for the pulsars. In year 2015, Fermi team released Pass 8 data including many improvements. Including better energy measurement and significantly improved effective area. Additionally, we have more *Fermi LAT* data. As a result, it is reasonable to redo the gamma-ray analysis with the newer dataset and more observation data in order to gain more reliable results.

Therefore, my main objective is to use the new data to redo the gamma-ray analysis of the three MSPs mentioned above. Then, I will do a numerical simulation based on a theoretical model called two-layer model and test if the new observation data are consistent with the the predictions of the model. And finally, based on numerical simulations of the two-layer emission model, I will generate broadband spectra (including hard X-ray band and gamma-ray band) for all the three MSPs.

Chapter 2

Gamma-Ray Analysis

As mentioned before, because of very short rotation periods, MSPs usually have very small light cylinder compared with normal pulsars. As a result, their emission mechanisms are similar to normal pulsars, especially for my target objects — PSRs J0218+4232, B1937+21 and B1821-24, which are among the fastest spinning MSPs. Therefore, as normal pulsars, the three MSPs have broadband emissions so it is convenient to analyze the spectra properties of them in gamma-ray band.

2.1 Introduction to the *Fermi Gamma-ray Space Telescope*

The *Fermi Gamma-ray Space Telescope* was launched on June 11, 2008 and opened a new window of studying supermassive black-hole systems, pulsars and so on. Its original name was *Gamma-ray Large Area Space Telescope* (GLAST) and changed to *Fermi Gamma-ray Space Telescope* in honor of the great scientist Enrico Fermi.

The *Fermi Gamma-ray Space Telescope* contains two parts: *Gamma-ray Burst Monitor (GBM)* and *Large Area Telescope (LAT)* and the latter is the main instrument which is at least 30 times more sensitive than all gamma-ray telescopes launched before. I only use LAT for my purposes. Thus I focus on the LAT instrument, which contains four main subcomponents including tracker, calorimeter, anti-coincidence detector and data acquisition system. The reason why the telescope is designed in this way is that high-energy gamma-rays cannot be refracted by lens or mirrors. Therefore, the ways that the *Fermi LAT* and other gamma-ray telescopes operates are completely different.

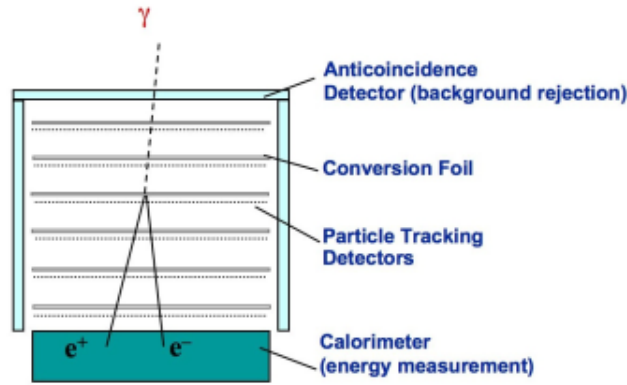


Figure 2.1: The figure (<https://www-glast.stanford.edu/instrument.html>) illustrates how *Fermi LAT* tracks incident gamma-ray photons.

Fig. 2.1 demonstrates the very basic idea of the *Fermi LAT* working principles.

- Gamma-ray photons can enter the anti-coincidence detector freely while cosmic-rays will generate signals which then tell the data acquisition system component to reject these particles. In this way, the *Fermi LAT* can distinguish the gamma-ray photons from high energy cosmic-rays and the confidence is over 99.9%.
- The conversion foil (shown in Fig. 2.1) can convert gamma-ray photons

into electron and positron pairs. This procedure makes it possible to determine the directions of the incident gamma-ray photons.

- The tracker (particle tracking detectors in Fig. 2.1) records the positions of the electrons and positrons generated from the gamma-ray photons. There are many trackers so the paths of a particles can be constructed by doing numerical simulations.
- When the electrons and positrons reach the calorimeter, their energies can be measured. By calculating the energy relationships between the gamma-ray photons and the correspond electrons and positrons, the energies of the original gamma-ray photons can also be obtained.
- The data acquisition system is like a filter of gamma-ray photons which can reject unwanted particles such as cosmic-rays. Also, photons come from the Earth's atmosphere are also rejected.

For a telescope, the ability of measuring the directions and energies of incident photons is very crucial. From the above descriptions of the *Fermi LAT* working principles, we know that the precision of construction of particles' paths heavily influences how well we can measure the directions and energies of gamma-ray photons. And this process is greatly dependent on simulation algorithms, which means that with the improvements of algorithms and datasets, the precision of the telescope can also be improved. The Pass 8 data have reprocessed the entire Fermi mission dataset so the quality of the dataset is much better. This is part of the reason why I redo the analysis of the three MSPs.

2.2 A Brief Introduction to Fermi Data Analysis

Brief Introduction to Intermediate Products

Instead of producing the final results directly, there are some intermediate procedures and corresponding products such as count maps, count cubes and so on as described below.

- A count map is basically generated by following steps. Firstly, we choose a pixel with a certain size. Then we check each photon's direction to determine if the photon is in this pixel. If it is in the pixel, the photon counts of the pixel will add one. Therefore the more photons fall within the pixel, the more photon counts the pixel has, hence the brighter the pixel is. By doing the same thing for every pixel in the ROI, a count map can be generated. A count map tells us know what we have observed intuitively and gives us a very basic idea of if we get the desired data.
- A count cube is very similar to a count map, except that a count cube contains many energy bands. For example, a dataset whose energy range is from 100MeV to 100GeV can be divided into 30 bins. We can generate a count map in each energy bin, thus we have 30 count maps. In other words, we can regard a count cube as a combination of multiple count maps. A count cube's advantage over a count map is that we can observe distribution of gamma-ray photons in different energy ranges.
- < mayAdd > may have more items < /mayAdd >

Processes of Doing Fermi Analysis

When doing *Fermi LAT* data analysis, I basically dealt with two parts. The first part is processing observation data and the second is generating photon distribution based on models. Cleaning data is straightforward including data selection, data filtering with good time intervals (GTIs), generating count maps and so on. Generating model-based count maps and count cubes needs a little bit more efforts and mainly includes the following procedures.

Firstly, I need to generate a spectra model of all sources in our region of interest (ROI). The model basically describes how strong each source is in different energy bands and different positions. The initial parameters of the model are from Fermi database. I do not fit positions of both point sources and diffuse sources when do the data analysis. However, the model alone is not very helpful and I have to know other informations in order to simulate photon distribution.

Since I am going to compare my simulation with the observation data, I have to take the telescope states into account. For example, the effective area of telescope decreases when away from the optical axis. In addition, inclination angles and observation time intervals have direct influences on the number of photon counts. In short, after I get the simulated photon distribution from our model, it is necessary to transfer the initial simulation into the real simulation by applying the telescope functions.

After obtaining the photon distributions and spectra simulations, I then can do comparisons in order to get the maximum likelihood. I divide the total energy band into many smaller energy bins and denote the number of photon counts in observation data as n_i , so that $\sum_i n_i = N$, where N is the total number of photons we have observed. The observed number of photon counts

in i th bin is a Poisson distribution with a mean of m_i . In fact, the value m_i is the expected number of photon counts from our spectra model. Therefore, the distribution for i th bin can be expressed by Eq. 2.1, where $P_i(n_i)$ is the possibility of observing the n_i photon counts for the i th bin.

$$P_i(n_i) = \frac{e^{-m_i} m_i^{n_i}}{n_i!} \quad (2.1)$$

As a result, it is not hard to generalize the possibility for each bin to all bins, just by multiplying the possibilities for different bins.

$$\begin{aligned} P_{total} &= \prod_i P_i(n_i) \\ &= e^{-\sum_i m_i} \prod_i \frac{m_i^{n_i}}{n_i!} \end{aligned} \quad (2.2)$$

In Eq. 2.2, n_i is directly from observation data so they usually can not be changed during the binned likelihood analysis. However, by changing the model, the m_i can be altered. Hence, my aim is to tweak the spectra model in order to make the total possibility P_{total} as large as possible.

This is the basic idea and procedure of doing Fermi data analysis. After doing these, we can go further such as testing how significant our targets are by creating TS maps. The thesis basically follows the procedures.

Before finishing this part, I should briefly introduce the basic idea of TS maps. TS stands for Test Statistic which can be expressed as Eq. 2.3

$$TS = -2 \ln \frac{L_{max,0}}{L_{max,1}} \quad (2.3)$$

where $L_{max,0}$ and $L_{max,1}$ are the maximum likelihood of models in which our target source is not included and included respectively. According to Eq. 2.3,

the larger the TS value is, the larger $L_{max,1}$ is, which means that the probability of existence of our target source is larger. In order to generate a TS map, we divide the whole map into many sub-grids. In each sub-grid, the algorithm basically does two things. The first procedure is calculating the maximum likelihood value directly based on our spectra model ($L_{max,0}$). Then it adds an imaginary source, fits the source and gets the maximum likelihood ($L_{max,1}$) value. Therefore, we have two maximum likelihood values. In the end, it calculate the TS value for the sub-grid according to Eq. 2.3.

After having the TS values for all sub-grids, we can generate a TS map just by rendering colors according to each grid's TS value. By comparing TS values of each grid in a TS map, we can determine where the target source is most likely to be and how large the probability is.

Generally speaking, for each source, I generate two TS maps and determine how likely my target source is observed. For instance, if the data show the source is observed, then the value of each pixel of the TS map containing the source should be low. On the contrary, the TS values of the pixels around the position of the target source should be significantly higher than other positions in the TS map.

2.3 *Fermi* LAT Data Analysis

The basic idea of fitting spectra parameters is to make the count cube generated by the model be as similar to the observation data as possible. The calculation process can be summarized as follows. First of all, we have to generate a spectral model for every source in the region of interest (ROI) based on the Fermi database. The database includes LAT four-year Point Source Cata-

log (3FGL), Galactic diffuse emission (gll_iem_v06.fits) and isotropic emission (iso_P8R2_SOURCE_V6_v06.txt). Then we can produce a count cube based on the model. Generally speaking, the difference of the count cubes between the model and observation is obvious. Then, the Fermi software adjusts the parameters to make the difference smaller. Until the errors are acceptable, the software outputs the final fitted parameters of corresponding spectral models.

We use a power-law with exponential-cutoff (PLExpCutoff) model to fit the observation data and it is a special case of the power-law with super-exponential-cutoff (PLSuperExpCutoff) model. The spectra of PLSuperExpCutoff can be described by Eq. 2.4:

$$\frac{dN}{dE} = N_0 \left(\frac{E}{E_0} \right)^{\gamma_1} \exp \left[- \left(\frac{E}{E_c} \right)^{\gamma_2} \right] \quad (2.4)$$

where N_0 is prefactor, E_c is the cutoff energy and the E_0 is a scale parameter. PLExpCutoff model is the special case where $\gamma_2 = 1$. My aim is to fit the parameters N_0 , E_c and γ_1 to make the model be more consistent with the observation data.

2.3.1 Verifying the Data Analysis Process

Before analyzing the observations of my target sources, it is reasonable to test if my procedures of data processing are right. In order to do so, I try to do analysis for two bright pulsars PSRs J0007+7303 and J0534+2200. The reason I choose these two pulsars is that according to previous studies, they are bright and easy to detect with a large TS value of 43388 and 102653 for J0007+7303 and J0534+2200 respectively. [1]

In the spectra fit process, I do not use the same fit parameters as the

previous paper, (for instance, the number of free parameters in the ROI is different) however, I get similar results in terms of spectra index. In Table 2.1, I used the observation data from 2009-01-01 to 2013-02-01 in order to try to be consistent with the old paper [1]. In addition, I also fit spectra with observation data up to 2018-02-01 and Pass 8 dataset to test how big improvement I can make with the new *Fermi Pass 8* dataset and more observation data. The results of year 2018 data are shown in Table 2.2.

Tables 2.1 and 2.2 mainly show two pieces of information. Firstly, my procedure of dealing with observation data has no big problems, so basically I can trust fit results of my target sources. Secondly, the *Fermi Pass 8 Lat Data* has improved the accuracy a lot. For example, as Table 2.1 shows, the photon indexes are 1.30 ± 0.02 and 1.4 ± 0.1 , which means that the errors reduce a lot. Additionally, the TS value is more than double as before. **<question>**However, the cutoff energies are not consistent between the previous result and the new result. (I need to explain this a little bit later).**</question>**

	Test Results			Previous Results		
	Γ	E_c (MeV)	TS	Γ	E_c (MeV)	TS
J0007+7303	1.30 ± 0.02	2010 ± 85	96979	1.4 ± 0.1	4700 ± 200	43388
J0534+2200	2.07 ± 0.01	9880 ± 572	239015	1.9 ± 0.1	4200 ± 200	102653

Table 2.1: The spectra fit results. In the thesis, in order to make data analysis more convinient, we use some pipeline scripts to deal with the observation data. The "Test Results" column shows the results generated by using the pipeline scripts. The "Previous Results" column lists the corresponding spectra properties based on the old paper [1]. According to the standard PLSuperExpCutoff model (described in equation 2.4, Γ is photon index and E_c is cutoff energy.)

	Γ	E_c (MeV)	TS
J0007+7303	1.34 ± 0.02	2204 ± 67	210166
J0534+2200	2.01 ± 0.01	9173 ± 372	449946

Table 2.2: Fit Results With Data From Year 2009 To Year 2018. The physical meanings of Γ and E_c are the same as Table 2.1.

2.3.2 PSR J0218+4232

The ROI is a circle with radius of 20° and all parameters of sources which are 8° outside of the center are fixed. For sources within 8° , initial values of parameters are the same as their default values. In my case, there are point sources which have free parameters. In Fig. 2.2, the green circles represent those free sources. There are some of very bright sources which have no free parameters in the outer parts of the count map. The reason is that they are so far away from the target source that the Fermi telescope can distinguish if a photon comes from the target source or the outer sources. As a result, we do not need to fit any parameters for those outer sources. However, it is another case for the nearby sources and we have to fit parameters of them.

Count Maps And Count Cubes

In the left of Fig. 2.2 is the count map of PSR J0218+4232. In the center of the left panel, we can clearly see our target source. The dimension of the figures seems to be weird and the reason why we have 141 pixels for both x and y axis is that we select a circle region from the original data. However, when we generate a count map, we have to assign the sizes for x and y axis separately, which means that our a count map is actually rectangular. As a result, we have to crop a rectangular from the original circle region and in this

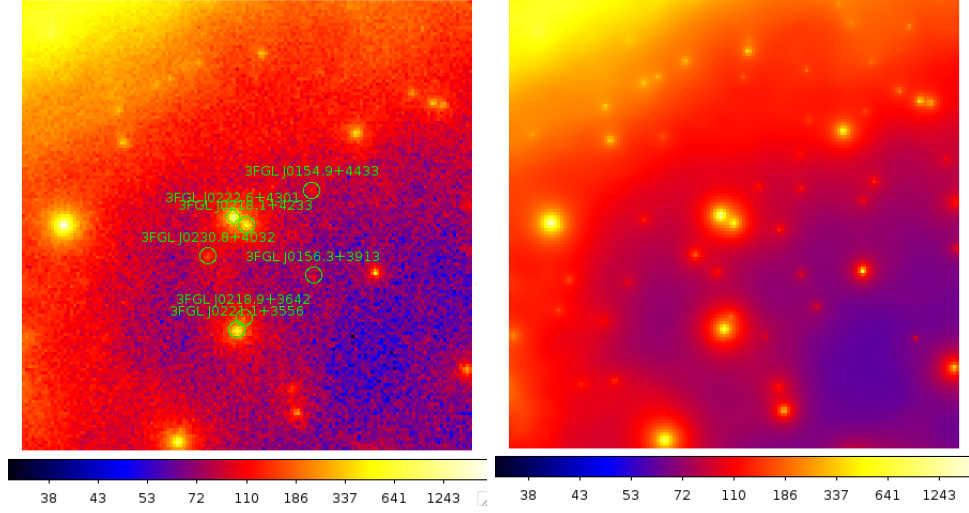


Figure 2.2: The count map of PSR J0218+4232 (left) and the count map generated by the model (right). In the left panel, the green circles represent free sources. Fig. in the right is a count map created according to our fitted spectra model. The size of each figure is $141 \text{ pixels} \times 141 \text{ pixels}$, and the dimension for each pixel is $0.2^\circ \times 0.2^\circ$.

case, we choose the rectangular as a square.

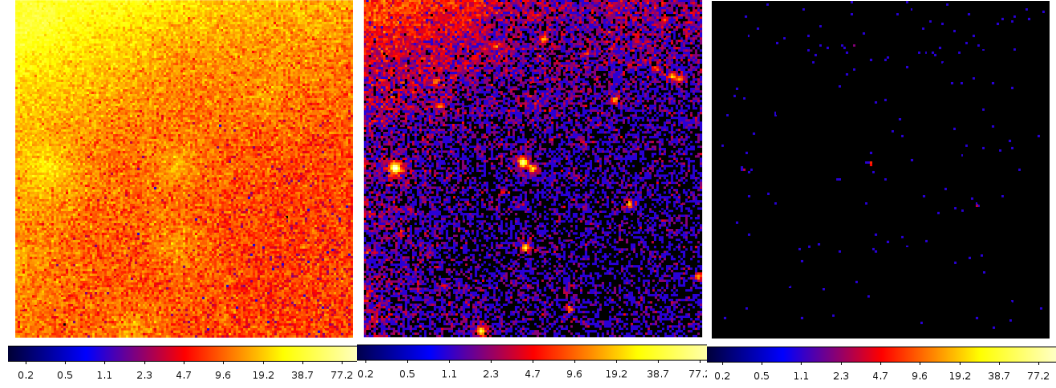


Figure 2.3: Three count maps from PSR J0218+4232's count cube. The energy ranges of the figures are 100~123MeV, 1.873~2.310GeV, 35.11~43.29GeV respectively.

Fig. 2.3 is a comparison between PSR J0218+4232's count maps in different energy bands. The count map in about 100MeV is so messy that we can hardly distinguish our target source while above 30GeV there are so few photons that there is not a clear sign of the source. We choose three circle regions whose

centers are the our target sources and the radii are 1000 " for all of the three figures and then calculate the total numbers of photon counts of the selected regions. As the following table 2.3 shows, though total number of photon counts around our target source is similar between the left and middle count maps, the numbers of counts per energy are much different. Since there are few photons in high energy bands (above 50 GeV) compare to other energy bands, we focus more on the lower energy part.

	Left	Middle	Right
Total counts	78	93	0
Energy range (MeV)	100~123	1873~2310	35110~43290
Counts / MeV (MeV^{-1})	3.39	0.213	0.000

Table 2.3: Numbers of photon counts of count maps in different energy bands for PSR J0218+4232.

Spectra Fitting

Fig. 2.2 shows that the fit result of the model is similar to the observation. However, there are lots of small red pixels in the left panel(generated directly by the observation data) while the right panel is very "clean". This means that a lot of photons are thought as generated by the modeled source. Thus in our model, the sources are generally slightly brighter than the observation. However, our target source is an exception. In the region we have used before (the center is the target source, and the radius is 1000"), the total photon count in the left panel is 1815 compare to 1737 in the right panel.

The reason why the count map generated directly by the observation data is a lot more messy is that our source model is generated according to the Fermi database and their spatial position is fixed. This means that if a photon comes

from a particular direction and there is no any known pulsar in that direction, this photon has to be classified to other directions and there is a modeled source in the direction. Thus, the spatial positions of photons are different between the observation and the model and the count maps generated directly from models are usually cleaner.

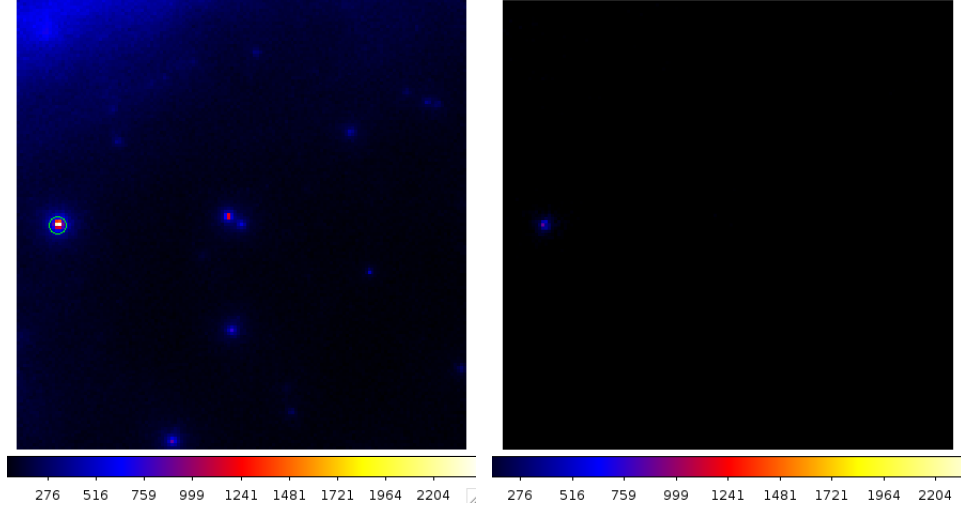


Figure 2.4: The count map and residual map of PSR J0218+4232. The figures are both in linear scale in order to compare the residual map between the original count map more intuitively. The left panel is the count map and the right one is the residual map which shows the differences between the observation and the spectral model. It is created by directly subtracting the photon counts of each pixel between the count maps of observation data and the spectral model. The green circle regions represent (the regions are completely the same in the two figures) the largest number photon counts of the residual map and its radius is $2000''$.

Fig. 2.4 basically describes how well our model is compared to the observation data. There are some black dots and bright dots in the residual map showing the differences between our spectral model and the observation data. In the residual map of Fig. 2.4, most differences of absolute photon counts are small, however, in the green circle region, the absolute value is large whose value is 6003. This means that in this region, the number of photon counts of the observation data (21525) is 6003 larger than in our model. This is not negligible since it is nearly 28% of the original photon counts. Does this mean

that our model is not good? The answer should be yes, however, this does not mean our fit is not good since the model parameters in this region are all fixed and the fixed values are from the Fermi LAT 4-year Point Source Catalog. Hence, the difference shows some problems of our spectral model, but has nothing to do with the fit result. Instead, from the residual map, we can see that the fit result is good because the differences of number of photon counts are very low, which are about 5% of the photon counts of the count map on average.

Table 2.4 lists the results of the fitting parameters. We see from Table 2.4 that the new fit results are consistent with the old results. However, the precision improves a lot which is ascribed to the Fermi LAT Third Source Catalogue and PASS 8 data. Fig. Function 2.4. One thing should be noticed is that we need to multiply E^2 to Function 2.4 fit is consistent with flux points fitted by each energy bin separately. The TS value of our target source is 7110, which gives us a significance level $\sigma \approx \sqrt{TS} = 84$. This strongly implies the presence of our target source. We can also use a TS map to test the presence of the source as Fig. 2.6 shows. There are two sets of Ts maps with different scales. The first group is $3^\circ \times 3^\circ$ while the second group is $2^\circ \times 2^\circ$.

	This Study		Previous Results	
	Value	Error	Value	Error
Index1 (γ_1)	1.89492	0.04044	2.0	0.1
Cutoff (E_c , MeV)	3766.69	397.38	4600	1200
Photon Flux (ph $cm^{-2}s^{-1}$) (10^{-8})	7.28913	0.27988	7.7	0.7

Table 2.4: Fit parameters of the spectral model of PSR J0218+4232. The names of parameters are consistent with Eq. 2.4. The old results are from the paper [1].

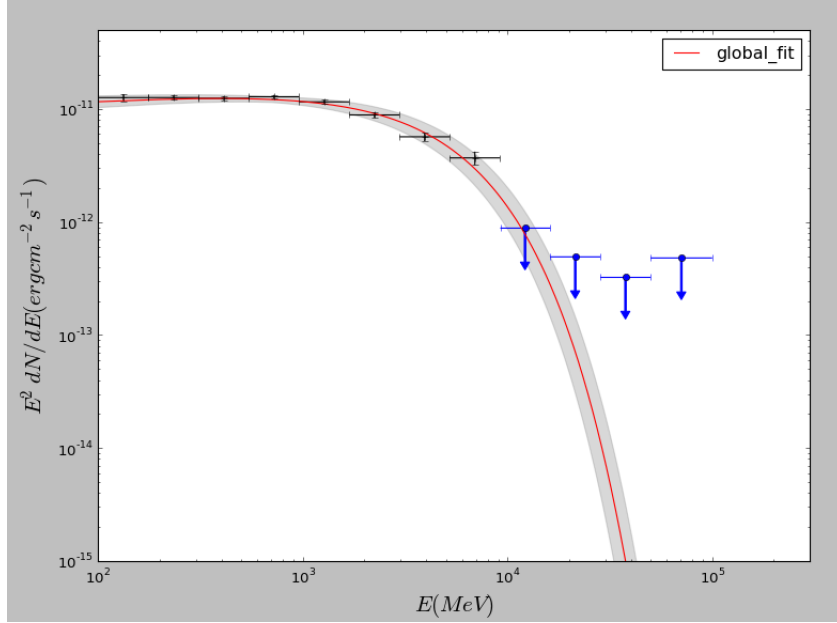


Figure 2.5: The log-log plot of flux to energy of PSR J0218+4232. The grey shade represents fitting errors, black points with error bars are flux points, the blue dots are upper values and the red line is the PLEXPcutoff model multiplied by E^2 . Flux points are fitted separately by dividing the total energy bin ($100 \text{ MeV} \sim 100 \text{ GeV}$) into multiple energy bins. The horizontal error bars represents the width of each bin.

2.3.3 PSR B1821-24

The ROI region is a circle whose radius is 20° and all parameters of sources outside of 8° are fixed. There are six free sources in the region of 8° . Fig. 2.7 is a combination of count maps of observation data and the model.

Count Maps And Count Cubes

The left and right part of Fig. 2.9 is the count map of the PSR B1821-24 generated from observation data and spectral model respectively. Like the situations of PSR J0218+4232, the count map from the model is clearly cleaner than from the observation data and the two figures are very similar, which implies that our model is close to the observation data.

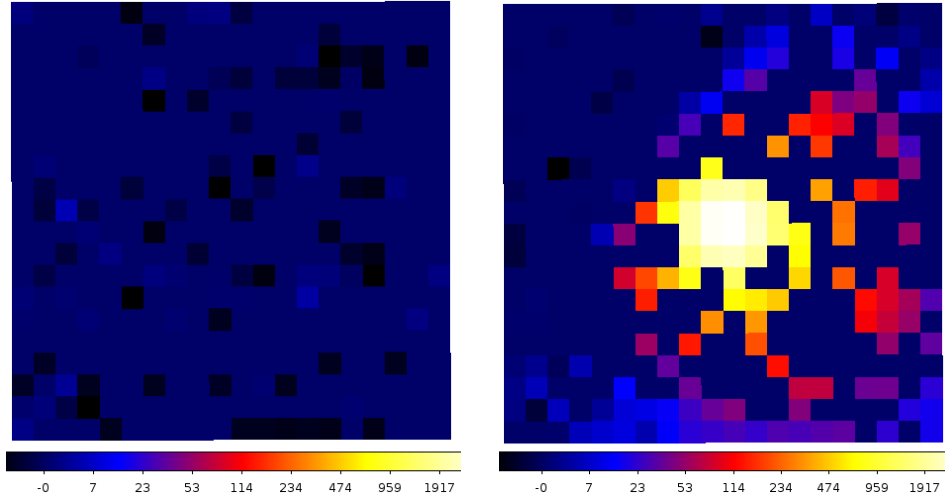


Figure 2.6: TS maps of PSR J0218+4232. Figures' dimensions are $4^\circ \times 4^\circ$ (20 pixels \times 20 pixels with $0.2^\circ \times 0.2^\circ$ for each pixel). The **left** figure and **right** figure are generated by the XML models with and without our target source PSR J0218+4232 respectively. The **left** figure shows that the possibility of adding an imputative point source is very low only with a maximum TS value of less than 5. However, the **right** figure strongly implies that there should be an additional source after we have removed our target source from the spectral model, which means it's highly likely that PSR J0218+4232 is contained in our observation data.

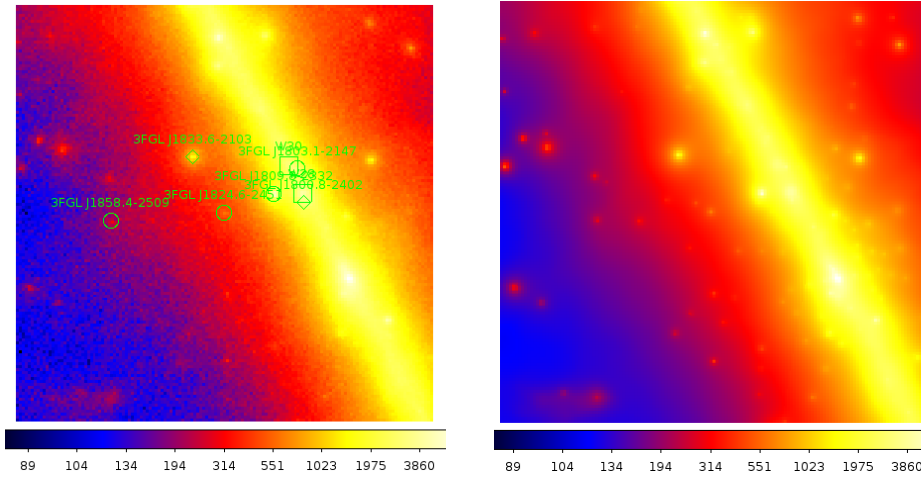


Figure 2.7: The count map of PSR B1821-24 (left) and the count map generated by the model (right). In the left panel, the green circles are free sources. The sizes of the both figures are 141 pixels \times 141 pixels, and each pixel's dimension is $0.2^\circ \times 0.2^\circ$.

Fig. 2.8 are count maps of PSR B1821-24 in different energy bands. The target pulsar is too faint in very high energy bands and interfered too much by

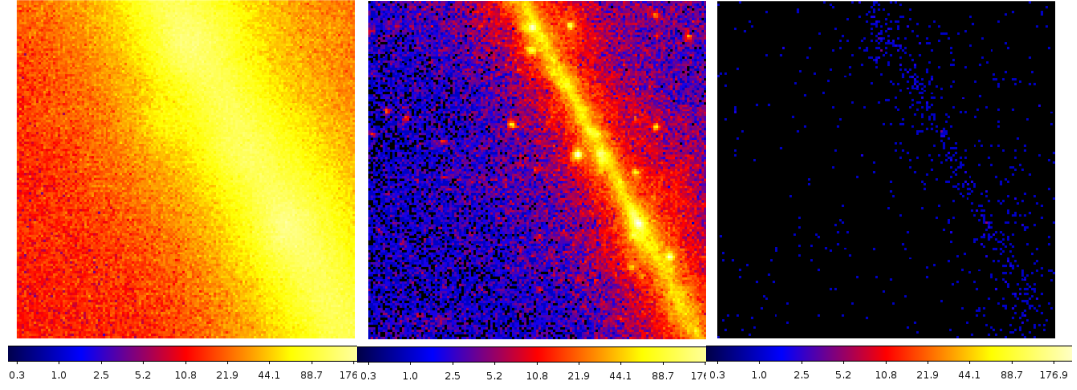


Figure 2.8: Three figures of PSR B1821-24's count cube. The energy ranges of the figures are 100~123MeV, 1.873~2.310GeV, 81.11~100GeV respectively from left to right.

the ambient environment in low energy bands (around 100MeV). Because our target source is near the M28 globular cluster and very faint, it is reasonable that the fitting result is not as good as PSR J0218+4232.

Binned Likelihood Analysis

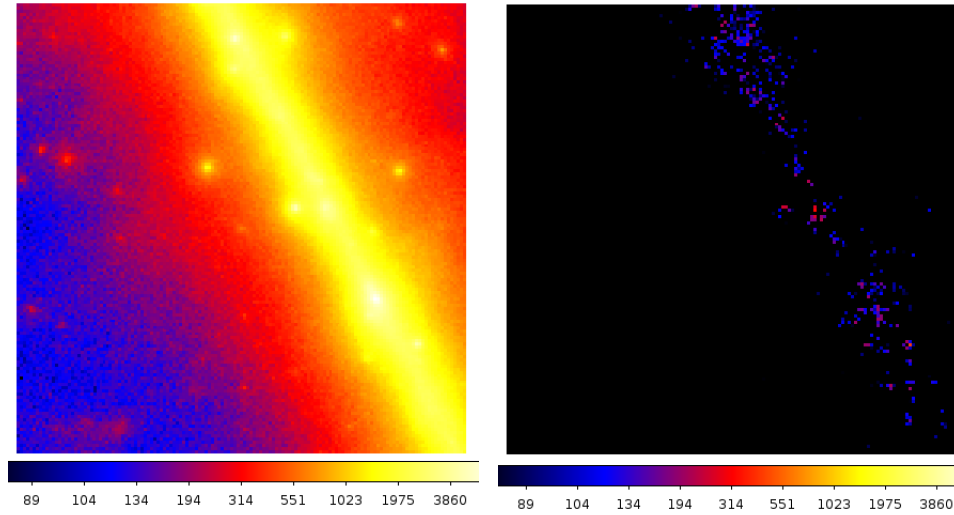


Figure 2.9: The count map and residual map of PSR B1821-24 in log scale. The reason why linear is not used here is that the residual map is nearly black in linear scale. The **left** figure is the count map and the **right** figure is the residual map showing the difference between the observation data and the spectral model.

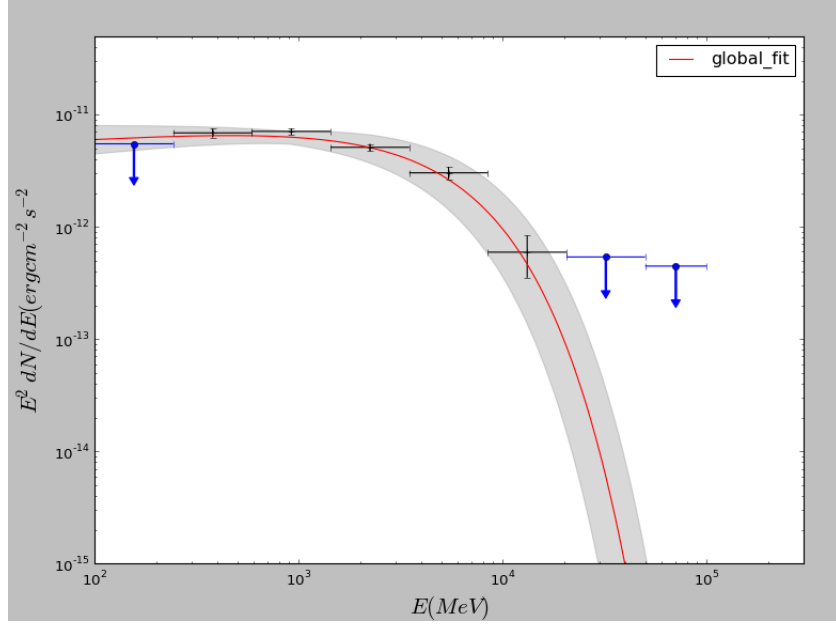


Figure 2.10: The log-log plot of flux to energy of PSR B1821-24's gamma-ray spectrum.

The differences of the count map between the observation data and the model are described as Fig. 2.9 which are both in linear scale. In the right part of Fig., there are some black dots with absolute values about -800 . Though their values are relatively high, the number of high-value dots are very small so the fit is acceptable in general.

Table 2.5 shows the global fit results of PSR B1821-24. The TS value of the model is 941 which gives us a significance level of about $\sqrt{941} \sim 31$. This strongly supports the existence of the target source in the observation data.

Fig. 3.3 shows that the global fit is consistent with the flux points generated by fitting sub-energy bins separately. However, we should notice the first flux point which is denoted as a blue square in Fig. 3.3. This flux point is significantly smaller than the global fit (the red line in Fig.). In addition, the upper value for the first energy bin is still slightly smaller than the global fit. Though it is strange that the upper value is smaller than the normal value at first glance, it is reasonable since the flux points are fitted separately and

are independent to the global fit. In fact, we use a single power-law model to fit each sub-energy bin while PLEXPcutoff model to do the global fit. As we have explained previously, the lower energy parts of the observation (around 100 MeV) is not as reliable as other energy bands. As a result, the separate fit for the first energy bin is not as reliable as the global fit and it is reasonable that the two fit results are not completely consistent. When this happening, we have more confidence on the global fit than the separate fit.

	This Study		Previous Results	
	Value	Error	Value	Error
Index1 (γ_1)	1.906	0.068	0.96	0.22
Cutoff (E_c , MeV)	4501.92	710.41	1410	300
Photon Flux ($\text{ph cm}^{-2}\text{s}^{-1}$) (10^{-8})	3.85	0.31	2.39	0.22

Table 2.5: Fit parameters of the spectral model of PSR B1821-24. The names of parameters are also onsistent with Eq. 2.4 We should note that the energy ranges of photon flux between the two results are different. The energy is from 100MeV to 100GeV for the new results while from 200MeV to 300GeV for the previous results.

2.3.4 PSR B1937+21

In order to make the data analysis be more consistent, we choose the same parameters to process the raw observation data. Like the other two MSPs, the radius of ROI is 20° degrees, and all parameters of sources 8° degrees outside from the center are fixed with default values. Fig. 2.12 is the comparison of count maps between observation data and the spectral model.

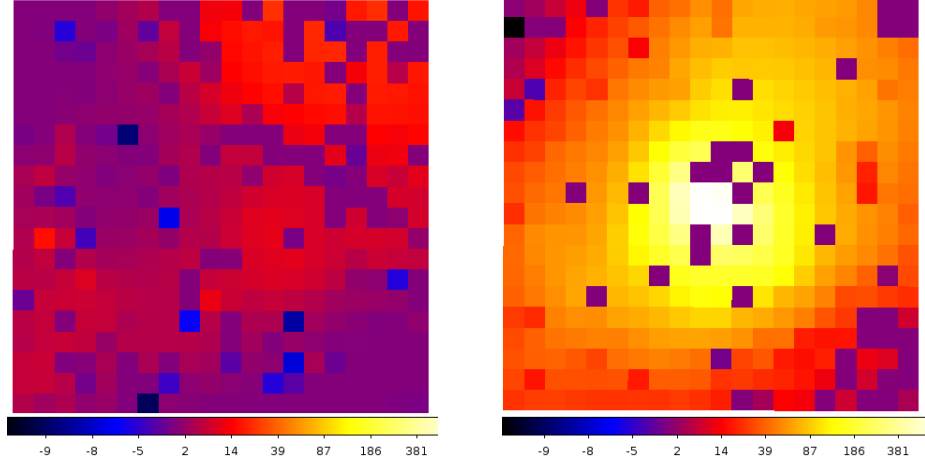


Figure 2.11: TS maps of PSR B1821-24. The figures' dimensions are $4^\circ \times 4^\circ$ (20 pixels \times 20 pixels with $0.2^\circ \times 0.2^\circ$ for each pixel). The **left** figure and **right** figure are generated by the XML models with and without our target source PSR B1821-24 respectively. The **left** figure shows that the possibility of adding an imputative point source is very low only with a maximum TS value of less than 11 while the TS values of the **right** figure are generally much larger.

Count Maps and Count Cubes

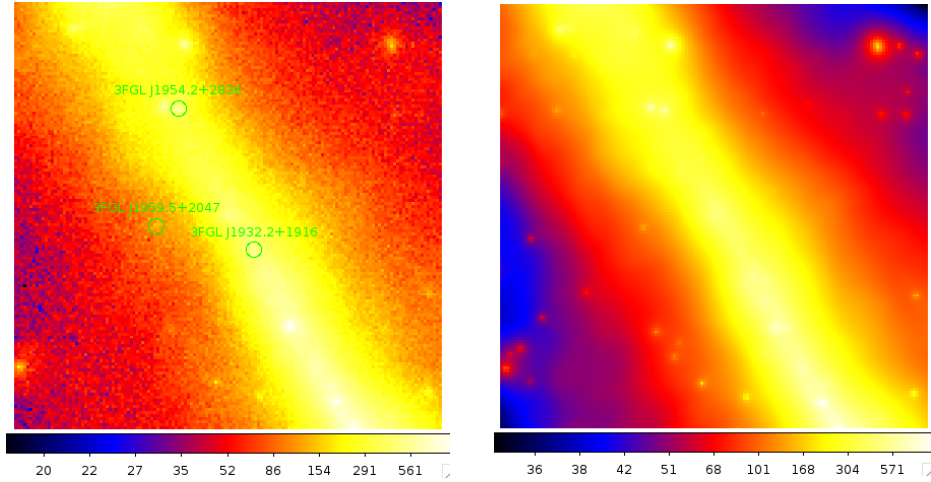


Figure 2.12: The count maps of PSR B1937+21 are created from observation data (**left**) and from the spectral model (**right**) respectively. The dimensions of both figures are $141\text{pixels} \times 141\text{pixels}$ and each pixel is $0.2^\circ \times 0.2^\circ$ large.

There are four point sources with free parameters in the model which are represented by the green circles in Fig. 2.12. However, the left panel

of Fig. 2.12 only contains three circles. This is the difference between the PSR B1937+21 and the other two MSPs discussed above. The PSR B1937+21 is not listed in the Fermi LAT Third Source Catalogue may be because that the MSP is so weak and the signal to noise ratio is very low that we could not get reliable spectrum fit results with a large TS value.

Therefore, in order to analyse the spectrum of the MSP, we have to add the source by hand. The green circles are only created by Fermi tools by default, hence our source is not represented by a green circle. In addition, the count map is so messy that we completely cannot identify the source PSR B1937+21 in the count map. Since our target PSR B1937+21 is not in the Fermi LAT Third Source Catalogue and we have to generate the model by hand, we need to initial the model with its parameters properly. Like the other two MSPs, we choose the specified PLSuperExpCutoff model and set the initial value of photon index to be -2.5 .

Fig. 2.14 shows count maps in difference energy bands. As the figure shows, the lower energy band is very messy while there is nearly nothing valuable in the high energy band. Therefore, when we divide the total energy bin into sub-bins to do analysis separately, we focus on the middle parts and have more bins in that range of energy.

<add>Continue from here...

PSR B1937+21 is a little bit different. I did a phase resolved analysis, in order to show if it is necessary, I plan to do a new phase averaged analysis for comparison. The best phase averaged results are not finished completely yet, but soon.</add>

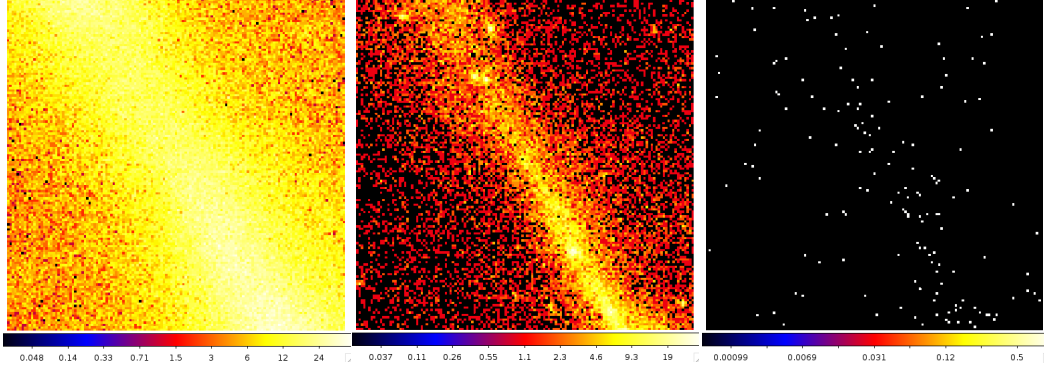


Figure 2.13: Three figures of PSR B1937+21's count cube. The energy ranges of the figures are 100~123MeV, 1.873~2.310GeV, 35.11~43.29GeV respectively.

Figure 2.14: here

Binned Likelihood Analysis

Fig. 2.15 is the residual map together with the original count map in linear scale.

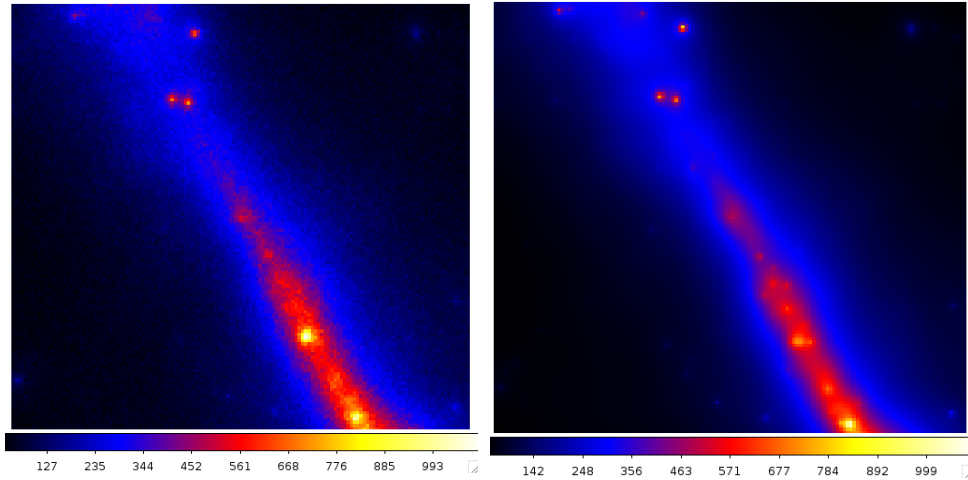


Figure 2.15: The count maps of PSR B1937+21 created from observation data (left) and from the spectral model (right). The dimensions of both figures are $141pixels \times 141pixels$ and each pixel's size is $0.2^\circ \times 0.2^\circ$.

Chapter 3

Theory And Simulation

3.1 Two-layer Model

After we have reviewed gamma-ray fundamental emission mechanism, we can proceed to the Two-layer model on which this thesis is mainly based. Two-layer model is a variation of outer-gap model since they both claim that the gamma-ray emission zone is close to the light-cylinder. However, in two-layer model, the outer layer consists of two regions — a primary acceleration region and a screening region.

In the primary region, charged particles moved out of pulsars along the open field lines, so the charge density is usually very low. However, by pair-production processes, a lot of e^- and e^+ are produced. But in the primary region where lots of pairs are created, the charge density doesn't change very much because the pairs have not been separated yet. With the help of strong electric field, the particles of different signs move to opposite directions. As a result, the two-layer model states that just above the primary region, a screening region will be created and the charge density is very large. This is

basically the reason why there are two regions in pulsars' outer magnetosphere.

Then the next issue is that how we describe the distribution of charge density in these two regions. For simplicity, we just use a step function to represent the charge density distribution and step function can clearly shows the gap between the two regions. We use a magnetic dipole model to approximate the magnetic distribution in the magnetosphere. Since in magnetic dipole model, magnetic fields at one position is only dependent on the position's distance from the source and altitude, we can also ignore the azimuthal distribution of charge density in our model and use the two parameters the distance r and altitude θ to calculate the magnetic field at some position.

In the two-layer model, we can use three parameters to express the structure of a pulsar's outer magnetosphere - charge density of the primary region, the total length of the primary region and the screening region and the last one is the ratio of the thickness of the primary region and the screening region. Fig. 3.1 shows the basic structure of two-layer model.

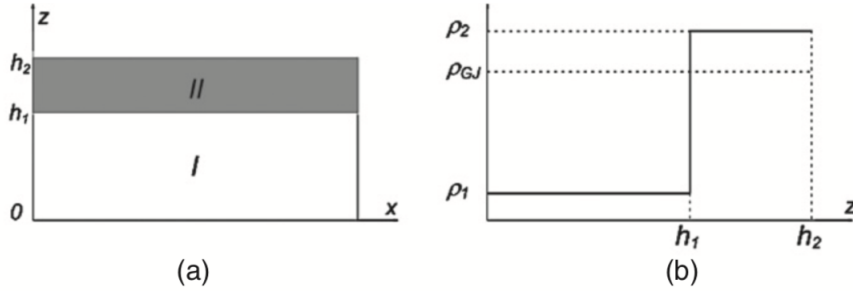


Figure 3.1: (a): Geometry of the two-layer model. h_1 and h_2 is the height of the primary region and the screening region respectively. (b): the charge densities of primary region and screening region. In the primary region, the charge density is much smaller than Goldreich-Julian charge density while is larger in the screening region.

As Fig. 3.1 shows, let the charge density of the primary region be $\rho_1 = (1 - g_1)\rho_{GJ}$ and the total gap size be h_2 , where ρ_{GJ} is the Goldreich-Julian charge density. For convenience, we also denote the gap size of the primary

region by h_1 .

We denote the electrical potential by ϕ_0 which satisfies

$$\nabla^2 \phi_0 = -4\pi \rho_{GJ} \quad (3.1)$$

and the total electrical potential is $\phi = \phi_0 + \phi'$, where ϕ' is a representation of the deviation of the co-rotating electrical potential. Let the total charge density be ρ and subtract Eq. 3.1 we have

$$\nabla^2 \phi' = -4\pi (\rho - \rho_{GJ}) \quad (3.2)$$

Because the model has ignored the distribution in the azimuthal direction, we can use two parameters x, z to represent a position, where x is the direction along the magnetic field line and z perpendicular to the magnetic field line. In order to solve Eq. 3.2, the model also makes two approximations. The first is that the directive of electrical potential ϕ is ignored. The second is that the Goldreich-Julian charge density is uniformly distributed along the magnetic line direction (x direction). These two approximations are based on a reasonable assumption that the change rate for both electrical potential (ϕ') and Goldreich-Julian charge density (ρ_{GJ}) along the x direction is much smaller compared with z direction. As a result, Eq. 3.2 can be written as:

$$\frac{\partial^2}{\partial z^2} \phi' = -4\pi (\rho - \rho_{GJ}) \quad (3.3)$$

In order to solve Eq. 3.3, we have to have proper boundary conditions. First of all, we have to decide the boundary positions, which is determined by four parameters and they are $x_{lo}, x_{hi}, z_{lo}, z_{hi}$. It is reasonable to set x_{lo} and

x_{hi} be the pulsar's surface and the light cylinder respectively and z_{lo} (lower boundary) be the last open field line. And let the electrical potential be 0 along the last open field line (this is because we have ignored the variation of electric field in x direction).

$$\phi(x, z_{lo}) = 0 \quad (3.4)$$

The position of z_{hi} is a little bit tricky. In order to make the electrical potential be continuous at $z = z_{hi} = h_2$, the model sets the $\phi'(z = h_2) = 0$ since the non-corotating electrical potential outside the upper bound is 0 and the co-rotating potential is continuous near the boundary. Additionally, because $\phi'(z = h_2-) = 0$ and $\phi'(z = h_2+) = 0$, we know that the first order derivative $\partial\phi'/\partial z|_{z=h_2}$ is 0, which means $E_\perp|_{z=h_2} = 0$. In order to solve Eq. 3.3, we denote charge densities of the two regions for convenience as the following function 3.5 shows.

$$\rho(z) = \begin{cases} \rho_1, & \text{if } (0 \leq z < h_1) \\ \rho_2, & \text{if } (h_1 \leq z \leq h_2) \end{cases} \quad (3.5)$$

With definition in Eq. 3.5 and the three boundary conditions we can directly solve Eq. 3.3 and the result is:

$$\phi'(z, x) = -2\pi \begin{cases} (\rho_1 - \rho_{GJ}(x)) z^2 + C_1 z, & (0 \leq z < h_1) \\ (\rho_2 - \rho_{GJ}(x)) (z^2 - h_2^2) + D_1 (z - h_2), & (h_1 \leq z \leq h_2) \end{cases} \quad (3.6)$$

where

$$C_1 = \frac{(\rho_1 - \rho_{GJ}(x)) h_1 (h_1 - 2h_2) - (\rho_2 - \rho_{GJ}(x)) (h_1 - h_2)^2}{h_2}$$

and

$$D_2 = \frac{(\rho_1 - \rho_2) h_1^2 - [\rho_2 - \rho_{GJ}(x)] h_2^2}{h_2}$$

From equation 3.6 and apply $\rho_{GJ}(x) = -(\Omega B x) / (2\pi cs)$ we can directly derive the electrical field parallel to magnetic field lines as a function of z as Eq. 3.7 shows.

$$E'_{\parallel}(z) = \frac{\Omega B}{cs} \begin{cases} -g_1 z^2 + C'_1 z, & (0 \leq z < h_1) \\ g_2 (z^2 - h_2^2) + D'_1 (z - h_2) & (h_1 \leq z \leq h_2) \end{cases} \quad (3.7)$$

where

$$C'_1 = \frac{g_1 h_1 (h_1 - 2h_2) + g_2 (h_1 - h_2)^2}{h_2}$$

and

$$D'_2 = -\frac{(g_1 + g_2) h_2^2 + g_2 h_2^2}{h_2}$$

Since charged particles are accelerated in the primary region to relativistic speed and then emit energy by curvature radiation, we have equation 3.8.

$$eE'_{\parallel} c = l_{cur} \quad (3.8)$$

where E'_{\parallel} is the electric field strength along the magnetic field line described in equation 3.7. We can estimate Lorentz factors of the charged particles according to Function 3.9.

$$l_{cur} = \frac{2e^2 c \gamma_e^4}{3s^2} \quad (3.9)$$

where s is the radius of curvature. Combining Eq. 3.8 and 3.9 we get Lorentz factor:

$$\gamma_e = \left(\frac{3s^2}{2e} E'_{\parallel} \right)^{1/4} \quad (3.10)$$

With Lorentz factor of charged particles known, we can derive curvature radi-

ation spectrum for single charged particle and then can get the total spectrum by integrating over all charged particles. This is the simplified basic idea of the Two-layer model.

Constraints of The Two-layer Model Used In The Thesis

The simplified two-layer model is consistent with observation data to some extent. (The relevant data can be found in the paper [9]) The model uses four parameters to get a fairly good prediction of the gamma-ray spectra of many pulsars. And all these four parameters have very obvious physical meanings. However, the problems of the model is clear — it is somewhat oversimplified. Although there are other more sophisticated versions of the two-layer model, I used the simpler one, which may cause some inconsistencies between the simulations and observations.

Therefore, we can briefly analyze which part is oversimplified and can be improved. First of all, we directly use a step function to describe the charged particle distribution. Though the charge density of the screening region is much larger than the primary region, using a step function is non-physical and may exaggerate the change rate of charge density. At the same time, the dramatic change of charge density also brings some instability for numerical simulation.

Secondly, the model sets the total of screening region and primary region to be rectangular shape. Though the shape is not clear, it should not be a rectangular in theory and may be very different. In numerical simulation, changes in shape of the regions will directly lead to a different integration region, which may change the simulated spectra completely.

Thirdly, there are some inconsistency in the model itself according to the

its assumption. According to Eq.s 3.9 and 3.10 since E'_{\parallel} can be 0, we know that γ_e can also be 0, which is absolutely impossible. Although this may not have a big influence on the spectra, it is the problem that we should solve.

All in all, the model is simple and the gamma-ray spectra computed based on the model is consistent with observation data. There are many much more sophisticated two-layer model which are generalizations of model used in the thesis. Those models may have addressed the problems described above, but the model used in the thesis do have some defects.

3.2 Numerical Calculation of Spectra Based on Two-layer Model

After we have understood the theory part of the two-layer model, we can then do numerical calculations of the spectra based on the theory. Since the theory is the same for all the three MSPs, the calculation algorithms are the same.

There are three independent parameters to fit altogether in the calculation. The first parameter is fractional gap size $f = h_2/R_{lc}$, where h_2 is the total gap size including both the primary acceleration region and the screening region and R_{lc} is the length of light cylinder. The second parameter is g_1 so that the charge density in the primary accelerating region is $(1 - g_1)\rho_{GJ}$, where ρ_{GJ} is the Goldreich-Julian charge density. The third parameter is the ratio between the sizes of the two gaps (h_1/h_2). Note that we only set the charge density in the primary acceleration region as an independent parameter, since the charge density in the two gaps are related to each other. Fig. 3.2 is the spectra of the three MSPs generated from the two-layer model and the result of the fitting parameters are listed in Table 3.1. Other than the low energy and high energy

gamma-ray bands, the model is consistent with the observation data in terms of gamma-ray part.

Generally speaking, the modeled spectra for the three MSPs are acceptable. Just as we have discussed in the data analysis part that global fits are not very consistent with separate fits in low energy gamma-ray band (about 100MeV – 1000MeV) and high energy band (above 10GeV), the modeled spectra also have the same problem. This can have two explanations. Firstly, the Fermi telescope is not sensitive below about 100MeV. As a result, the observation data may not be very reliable at this energy band. Secondly, the real emission mechanism in the energy band is different from the model predicts. Thus, we can observe inconsistency between the calculations and observations.

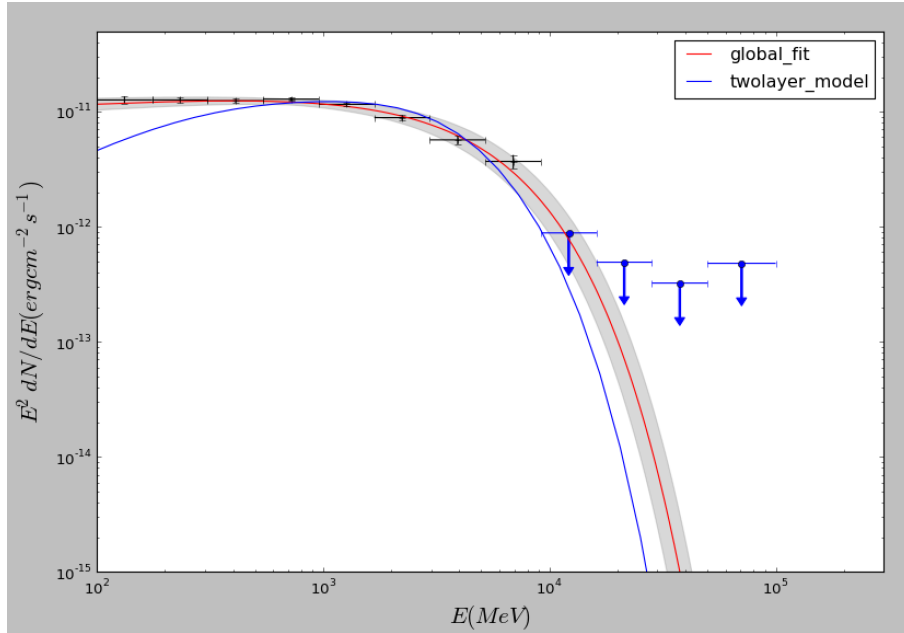


Figure 3.2: The modeled spectrum of PSR J0218+4232.

After obtaining the spectra fit results in gamma-ray band, we can generate broad band spectra as Fig. 3.5 shows. The hard X-ray data are from the paper [2]. By tweaking the independent parameters of the two-layer model, we can make the modeled spectra very close to the observation data in hard X-ray

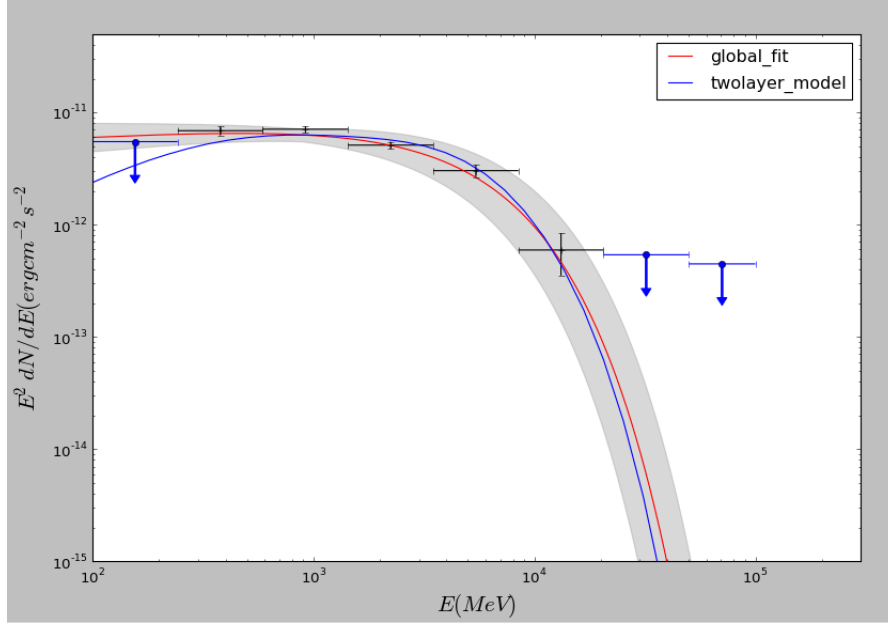


Figure 3.3: The modeled spectrum of PSR B1821-24.

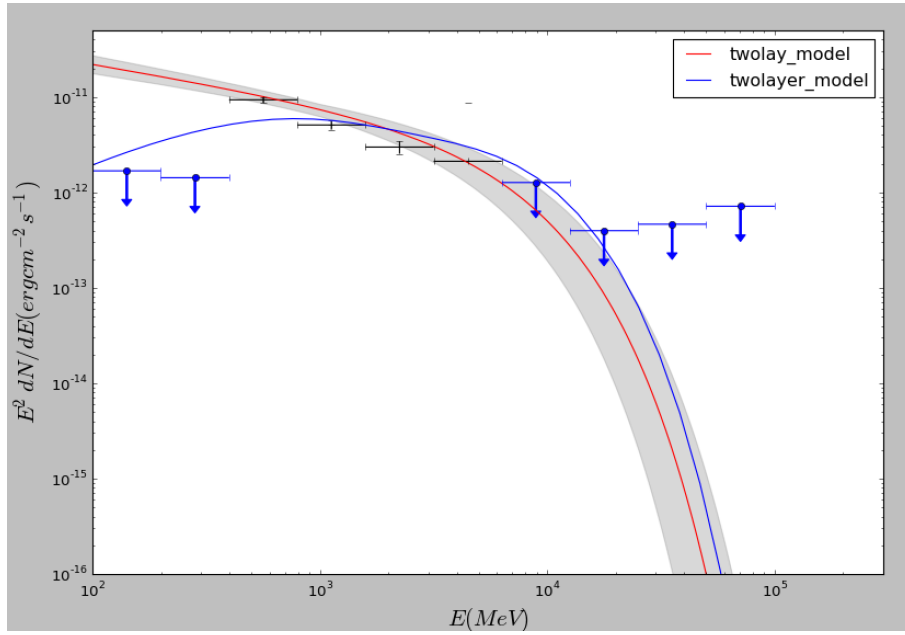


Figure 3.4: The modeled spectrum of PSR B1937+21.

band. Since we lack observation data in the energy band from about 100keV to 100MeV, we cannot tell if the two-layer model describes the right physical scenario in this energy range. However, the prediction made by the simplified two-layer model is relatively precise. In addition, the model is very intuitive, which is also a very important consideration for building a model. Just as the

	f	g	h_1/h_2
PSR J0218+4232	0.330	0.92	0.915
PSR B1821-24	0.247	0.955	0.920
PSR B1937+21	0.320	0.975	0.925

Table 3.1: The results of fitting parameters for the three MSPs. The physical meaning of each parameter is consistent with the two-layer model describe above.

famous words "With four parameters I can fit an elephant, and with five I can make him wiggle his trunk" said by John von Neumann, in principal, we can fit any data by adding independent parameters. Therefore, in order to test if a theory model is good or not, not only we need to consider how precisely the model can predict, but also the physical meaning behind the model. In this sense, the two-layer model is a good start of explaining emission mechanism of pulsars.

3.3 Pitfalls and Considerations of Doing Numerical Calculation

3.3.1 Correctness of Computation

To make sure the numerical computation be right is the most important. The first consideration is underflow and overflow of floating digits. One possible condition is calculating speed of relativistic charged particles with Lorentz

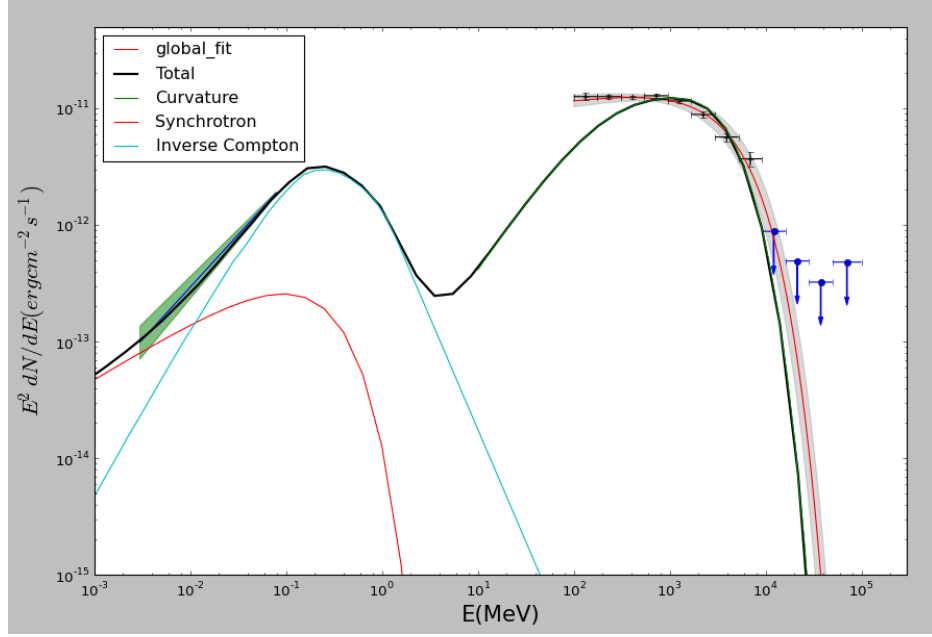


Figure 3.5: The broad band and modeled spectrum of PSR J0218+4232. The grey shade is the error of the global fit. And the green shade in the left panel of the figure represents the error of hard X-ray. The 'Total' legend represents the total flux combining the Synchrotron radiation, inverse Compton radiation and curvature radiation altogether.

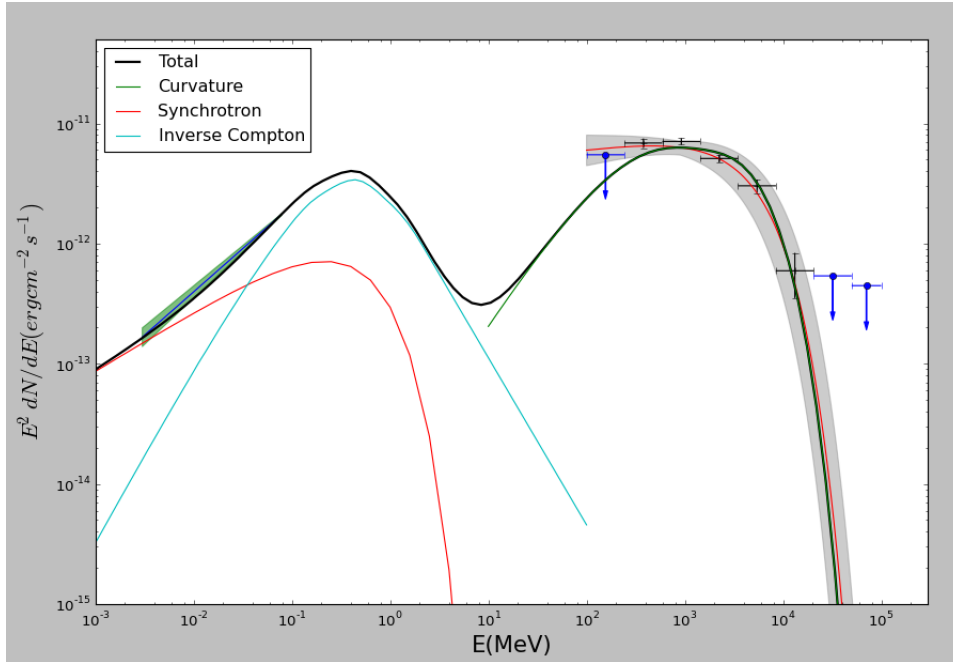


Figure 3.6: The broad band and modeled spectrum of PSR B1821-24. The meaning of grey shade and the green shade are the same as Fig. 3.5

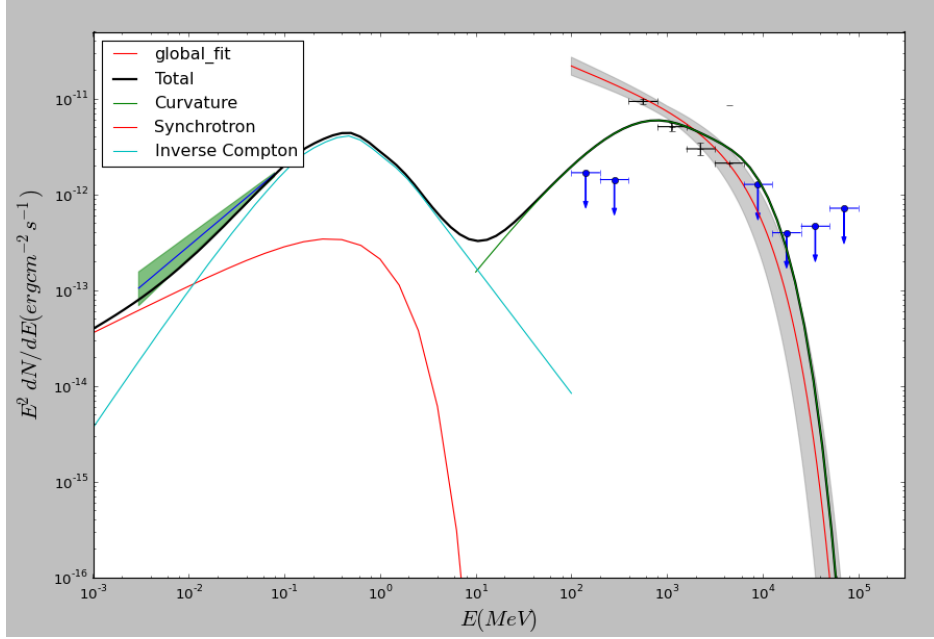


Figure 3.7: The broad band and modeled spectrum of PSR B1937+21. The meaning of grey shade and the green shade are the same as Fig. 3.5

factor γ . By doing some simple test, we find that for $\gamma < 1.5 \times 10^7$, the results are precise enough. However, there is significant rounding error when $\gamma > 5 \times 10^7$, which means that our results will be wrong for highly energetic particles if we directly use the formula $\beta = \sqrt{1 - 1/\gamma^2}$. Likely, in the two-layer model, nearly all particles have $\gamma < 1 \times 10^7$. Furthermore, there are nearly no situations where double precision floating digits cannot handle calculation results of the two-layer model. Thus, as long as we use 64-bit floating digits instead of 32-bit floating digits, we are free from overflowing and underflow troubles.

There are some cases when a whole function can be calculated while some parts of them are not. Take Function $f(x) = x \times 1/x$ for example. When x is too large, it can not be expressed by a computer and multiplication is not associative when doing floating point operation. We encounter some situations like this. The formula of curvature radiation spectrum contains modified Bessel function of order $5/3$. In order to speed up the program, we use a polynomial

to express the Bessel function, as Eq. 3.11 shows.

$$K_{5/3}(x) \simeq a \left(\frac{1}{x} + b \right)^{-cx-1/3} \sqrt{\frac{\pi}{2}} e^{-x-d} \sqrt{x+d} \left[1 + \frac{55}{72(x+d)} - \frac{10151}{10368} (x+d)^2 \right] \quad (3.11)$$

where a, b, c, d are just positive constants and $c = 0.96 < 1$. As a result, the part $(1/x + b)^{-cx-1/3}$ in Function 3.11 is infinity when x is large though the total function is approximated to 0. Thus, we have to explicitly assign the result to be 0 instead of calculating it. Actually, this error is not easy to find since in most cases the result is not infinity.

3.3.2 Speed of Computation

We actually have not done any accurate benchmarks for the following discussions and they are dependent of the average time of running the simulation. The most obvious solution of to use multicores to do computation. However, most library functions do not support run concurrently and only run on a single core. For example, we need to do many integrations and the speed of integration is critical. We write some simple functions to utilize four CPU cores at the same time when doing integration. This gives us a huge performance improvement.

Furthermore, There are some facts about the basic operations. For instance, add is faster than multiplication which is faster than devision. Multiplications and devisions are not associative between floating points. Though the performance differences between different operations for integers can usually be optimized away by modern compilers, the compilers can do nothing for floating points. Thus, we have to do it by ourselves. For example, we have $z^2 - h_2(x)^2$ in function 3.7. In this formula, we have two multiplications and one subtraction. After we re-write it to $(z - h_2)(z + h_2)$, we have one addi-

tion, one subtraction and one multiplication. Since addition and subtraction is not slower than multiplication, it has no performance harm for the rewriting. What we need to notice is that the multiplication may not be slower than addition and it is dependent on machines. However, division is definitely slower than the other three operations. Therefore, in our program, expressions like $1/3$ are rewritten to $1 * 0.3333$ and so on.

Chapter 4

Discussion and Future Work

<add>continue from here...</add>

Bibliography

- [1] A. A. Abdo, M. Ajello, A. Allafort, L. Baldini, J. Ballet, G. Barbiellini, M. G. Baring, D. Bastieri, A. Belfiore, R. Bellazzini, B. Bhattacharyya, E. Bissaldi, E. D. Bloom, E. Bonamente, E. Bottacini, T. J. Brandt, J. Bregeon, M. Brigida, P. Bruel, R. Buehler, M. Burgay, T. H. Burnett, G. Busetto, S. Buson, G. A. Caliandro, R. A. Cameron, F. Camilo, P. A. Caraveo, J. M. Casandjian, C. Cecchi, Ö. Çelik, E. Charles, S. Chaty, R. C. G. Chaves, A. Chekhtman, A. W. Chen, J. Chiang, G. Chiaro, S. Ciprini, R. Claus, I. Cognard, J. Cohen-Tanugi, L. R. Cominsky, J. Conrad, S. Cutini, F. D’Ammando, A. de Angelis, M. E. DeCesar, A. De Luca, P. R. den Hartog, F. de Palma, C. D. Dermer, G. Desvignes, S. W. Digel, L. Di Venere, P. S. Drell, A. Drlica-Wagner, R. Dubois, D. Dumora, C. M. Espinoza, L. Falletti, C. Favuzzi, E. C. Ferrara, W. B. Focke, A. Franckowiak, P. C. C. Freire, S. Funk, P. Fusco, F. Gargano, D. Gasparrini, S. Germani, N. Giglietto, P. Giommi, F. Giordano, M. Giroletti, T. Glanzman, G. Godfrey, E. V. Gotthelf, I. A. Grenier, M.-H. Grondin, J. E. Grove, L. Guillemot, S. Guiriec, D. Hadasch, Y. Hanabata, A. K. Harding, M. Hayashida, E. Hays, J. Hessels, J. Hewitt, A. B. Hill, D. Horan, X. Hou, R. E. Hughes, M. S. Jackson, G. H. Janssen, T. Jogler, G. Jóhannesson, R. P. Johnson, A. S. Johnson, T. J. Johnson, W. N. Johnson, S. Johnston, T. Kamae, J. Kataoka, M. Keith, M. Kerr, J. Knödseder, M. Kramer, M. Kuss, J. Lande, S. Larsson, L. Latronico, M. Lemoine-

Goumard, F. Longo, F. Loparco, M. N. Lovellette, P. Lubrano, A. G. Lyne, R. N. Manchester, M. Marelli, F. Massaro, M. Mayer, M. N. Mazzotta, J. E. McEnery, M. A. McLaughlin, J. Mehault, P. F. Michelson, R. P. Mignani, W. Mitthumsiri, T. Mizuno, A. A. Moiseev, M. E. Monzani, A. Morselli, I. V. Moskalenko, S. Murgia, T. Nakamori, R. Nemmen, E. Nuss, M. Ohno, T. Ohsugi, M. Orienti, E. Orlando, J. F. Ormes, D. Paneque, J. H. Panetta, D. Parent, J. S. Perkins, M. Pesce-Rollins, M. Pierbattista, F. Piron, G. Pivato, H. J. Pletsch, T. A. Porter, A. Possenti, S. Rainò, R. Rando, S. M. Ransom, P. S. Ray, M. Razzano, N. Rea, A. Reimer, O. Reimer, N. Renault, T. Reposeur, S. Ritz, R. W. Romani, M. Roth, R. Rousseau, J. Roy, J. Ruan, A. Sartori, P. M. Saz Parkinson, J. D. Scargle, A. Schulz, C. Sgrò, R. Shannon, E. J. Siskind, D. A. Smith, G. Spandre, P. Spinelli, B. W. Stappers, A. W. Strong, D. J. Suson, H. Takahashi, J. G. Thayer, J. B. Thayer, G. Theureau, D. J. Thompson, S. E. Thorsett, L. Tibaldo, O. Tibolla, M. Tinivella, D. F. Torres, G. Tosti, E. Troja, Y. Uchiyama, T. L. Usher, J. Vandenbroucke, V. Vasileiou, C. Venter, G. Vianello, V. Vitale, N. Wang, P. Weltevrede, B. L. Winer, M. T. Wolff, D. L. Wood, K. S. Wood, M. Wood, and Z. Yang. The second fermi large area telescope catalog of gamma-ray pulsars. *The Astrophysical Journal Supplement Series*, 208(2):17, 2013.

- [2] E. V. Gotthelf and S. Bogdanov. Nustar hard x-ray observations of the energetic millisecond pulsars psr b1821-24, psr b1937+21, and psr j0218+4232. *The Astrophysical Journal*, 845(2):159, 2017.
- [3] L. Guillemot, T. J. Johnson, C. Venter, M. Kerr, B. Pancrazi, M. Livingstone, G. H. Janssen, P. Jaroenjittichai, M. Kramer, I. Cognard, B. W. Stappers, A. K. Harding, F. Camilo, C. M. Espinoza, P. C. C. Freire, F. Gargano, J. E. Grove, S. Johnston, P. F. Michelson, A. Noutsos, D. Par-

- ent, S. M. Ransom, P. S. Ray, R. Shannon, D. A. Smith, G. Theureau, S. E. Thorsett, and N. Webb. Pulsed gamma rays from the original millisecond and black widow pulsars: A case for caustic radio emission? *The Astrophysical Journal*, 744(1):33, 2012.
- [4] O. Hamil, J. R. Stone, M. Urbanec, and G. Urbancová. Braking index of isolated pulsars. *Phys. Rev. D*, 91:063007, Mar 2015.
- [5] C.-Y. Ng, J. Takata, G. C. K. Leung, K. S. Cheng, and P. Philippopoulos. High-energy emission of the first millisecond pulsar. *The Astrophysical Journal*, 787(2):167, 2014.
- [6] Zakir F. Seidov. The roche problem: Some analytics. *The Astrophysical Journal*, 603(1):283, 2004.
- [7] P. A. Sturrock. A model of pulsars. *Astrophys. J.*, 164:529, 1971.
- [8] Hao Tong. Pulsar braking: magnetodipole vs. wind. *Science China Physics, Mechanics Astronomy*, 59(1):619501.
- [9] Y. Wang, J. Takata, and K. S. Cheng. Gamma-ray spectral properties of mature pulsars: A two-layer model. *The Astrophysical Journal*, 720(1):178, 2010.